Laboratory Evaluation of Corrosion Resistance of Various Metallic Dowel Bars

PUBLICATION NO. FHWA-HRT-15-079

JUNE 2018

U.S. Department of Transportation
Federal Highway Administration

Research, Development, and Technology
Turner-Fairbank Highway Research Center
6300 Georgetown Pike
McLean, VA 22101-2296

FOREWORD

This report presents findings on a corrosion study related to the corrosion resistance of eight types of metallic dowel bars. The accelerated laboratory corrosion testing was performed using seven small-scale concrete slabs that simulated typical concrete pavements for 452 d of a modified Southern Exposure followed by a detailed autopsy of the extracted bar samples. The best corrosion performance was achieved by type 316L solid stainless steel (SS) dowel bars. Three types of stainless steel–clad bars also exhibited superior corrosion resistance. The epoxy-coated dowel bars performed well and behaved similarly to the SS bar types despite varying degrees of coating delamination and localized corrosion originating from some of the artificial coating defects.

The target audience of this report is State transportation departments, city and county engineers, pavement researchers, and consulting firms.

Cheryl Allen Richter, P.E., Ph.D.
Director, Office of Infrastructure
Research and Development

TECHNICAL REPORT DOCUMENTATION PAGE

1. Report No. FHWA-HRT-15-079	2. Government Accession No.	3. Recipient's Catalog No.
4. Title and Subtitle Laboratory Evaluation of Corrosion Resistance of Various Metallic Dowel Bars		5. Report Date June 2018 6. Performing Organization Code
7. Author(s) Seung-Kyoung Lee		8. Performing Organization Report No.
9. Performing Organization Name and Address SK Lee & Associates, Inc. Fairfax, VA 22030 Rutgers, The State University 100 Brett Road Piscataway, NJ 08854		10. Work Unit No. Center for Advanced Infrastructure and Transportation (CAIT) 11. Contract or Grant No. DTFH61-08-C-00005
12. Sponsoring Agency Name and Address Office of Infrastructure Research and Development Turner-Fairbank Highway Research Center Federal Highway Administration 6300 Georgetown Pike McLean, VA 22101-2296		13. Type of Report and Period Covered Final report; January 2006–August 2015 14. Sponsoring Agency Code HRDI-60

15. Supplementary Notes
The Federal Highway Administration Technical Contact is Donald Becker (HRDI-10) and the Contracting Officer's Representative is R. Zobel (HRDI-30).

16. Abstract
This report presents corrosion study findings related to corrosion resistance of eight types of metallic dowel bars. The accelerated laboratory corrosion testing was performed using seven small-scale concrete slabs that simulated typical concrete pavements for 452 d of a modified Southern Exposure followed by a detailed autopsy of the extracted bar samples. The weekly Southern Exposure cycles consisted of a 4-d wetting cycle in 15 weight percent chloride solution at 75 °F and a 3-d drying cycle at 100 °F. The best corrosion performance was achieved by type 316L solid stainless steel (SS) dowel bars. Three types of stainless steel–clad (SC) bars also exhibited superior corrosion resistance. The epoxy-coated (EC) dowel bars performed well and behaved similarly to the SS bar types. However, the autopsied EC dowel bars revealed varying degrees of coating delamination, and localized corrosion originated from some of the artificial coating defects. Despite this problem, EC dowel bars were able to suppress corrosion activities because of the shielding role of the coating, even disbonded EC dowel bars, against corrosion current. As expected, the worst corrosion performance was observed with the uncoated carbon steel dowel bars. Most of them produced the corrosion-induced concrete cracks. The hot-dip galvanized and zinc-clad dowel bars are classified as the second worst performance group. Even though the zinc-coating layers performed well as the sacrificial cathodic protection systems for the bare steel exposed at the artificial defect sites, the consumption rates of the zinc mass were too excessive, leading to the premature depletion of the zinc layers in the areas with elevated chloride concentration. Therefore, these zinc-based dowel bars are recommended only for infrequently salted roadways and mild service conditions. For major roadways, where repairs and/or traffic disruption are not feasible, high grades of solid SS dowel bars are recommended, even though this means very high initial costs. Considering the unavailability of the SC bars and the good performance of EC dowel bars at a much lower price, it is recommended that high-quality EC dowel bars be continuously used in the majority of the major roadways subject to heavy deicing salts provided that damage touchups and stringent quality assurance/quality control practices are implemented in the field to minimize initial coating defects until they are buried in concrete.

17. Key Words	18. Distribution Statement
Corrosion, corrosion resistant metallic dowel bars, chloride threshold, corrosion initiation, corrosion propagation, autopsy, accelerated corrosion testing	No restrictions. This document is available to the public through the National Technical Information Service, Springfield, VA 22161. http://www.ntis.gov

19. Security Classif. (of this report)	20. Security Classif. (of this page)	21. No of Pages	22. Price
Unclassified	Unclassified	92	

Form DOT F 1700.7 (8-72) Reproduction of completed pages authorized.

SI* (MODERN METRIC) CONVERSION FACTORS

APPROXIMATE CONVERSIONS TO SI UNITS

Symbol	When You Know	Multiply By	To Find	Symbol
		LENGTH		
in	inches	25.4	millimeters	mm
ft	feet	0.305	meters	m
yd	yards	0.914	meters	m
mi	miles	1.61	kilometers	km
		AREA		
in^2	square inches	645.2	square millimeters	mm^2
ft^2	square feet	0.093	square meters	m^2
yd^2	square yard	0.836	square meters	m^2
ac	acres	0.405	hectares	ha
mi^2	square miles	2.59	square kilometers	km^2
		VOLUME		
fl oz	fluid ounces	29.57	milliliters	mL
gal	gallons	3.785	liters	L
ft^3	cubic feet	0.028	cubic meters	m^3
yd^3	cubic yards	0.765	cubic meters	m^3
	NOTE: volumes greater than 1000 L shall be shown in m^3			
		MASS		
oz	ounces	28.35	grams	g
lb	pounds	0.454	kilograms	kg
T	short tons (2000 lb)	0.907	megagrams (or "metric ton")	Mg (or "t")
		TEMPERATURE (exact degrees)		
^oF	Fahrenheit	5 (F-32)/9 or (F-32)/1.8	Celsius	^oC
		ILLUMINATION		
fc	foot-candles	10.76	lux	lx
fl	foot-Lamberts	3.426	$candela/m^2$	cd/m^2
		FORCE and PRESSURE or STRESS		
lbf	poundforce	4.45	newtons	N
lbf/in^2	poundforce per square inch	6.89	kilopascals	kPa

APPROXIMATE CONVERSIONS FROM SI UNITS

Symbol	When You Know	Multiply By	To Find	Symbol
		LENGTH		
mm	millimeters	0.039	inches	in
m	meters	3.28	feet	ft
m	meters	1.09	yards	yd
km	kilometers	0.621	miles	mi
		AREA		
mm^2	square millimeters	0.0016	square inches	in^2
m^2	square meters	10.764	square feet	ft^2
m^2	square meters	1.195	square yards	yd^2
ha	hectares	2.47	acres	ac
km^2	square kilometers	0.386	square miles	mi^2
		VOLUME		
mL	milliliters	0.034	fluid ounces	fl oz
L	liters	0.264	gallons	gal
m^3	cubic meters	35.314	cubic feet	ft^3
m^3	cubic meters	1.307	cubic yards	yd^3
		MASS		
g	grams	0.035	ounces	oz
kg	kilograms	2.202	pounds	lb
Mg (or "t")	megagrams (or "metric ton")	1.103	short tons (2000 lb)	T
		TEMPERATURE (exact degrees)		
^oC	Celsius	1.8C+32	Fahrenheit	^oF
		ILLUMINATION		
lx	lux	0.0929	foot-candles	fc
cd/m^2	$candela/m^2$	0.2919	foot-Lamberts	fl
		FORCE and PRESSURE or STRESS		
N	newtons	0.225	poundforce	lbf
kPa	kilopascals	0.145	poundforce per square inch	lbf/in^2

*SI is the symbol for the International System of Units. Appropriate rounding should be made to comply with Section 4 of ASTM E380.
(Revised March 2003)

TABLE OF CONTENTS

LIST OF FIGURES

LIST OF TABLES

LIST OF ABBREVIATIONS AND SYMBOLS

Abbreviations

AASHTO	American Association of State and Highway Transportation Officials
AC	alternating current
CS	carbon steel
CV	coefficient of variation
EC	epoxy-coated
ECR	epoxy-coated reinforcing
EIS	electrochemical impedance spectroscopy
FRP	fiber-reinforced polymer
HDG	hot-dip galvanized
HPC	high-performance concrete
JPCP	jointed plain concrete pavement
JRCP	jointed reinforced concrete pavement
LPR	linear polarization resistance
LTE	load transfer efficiency
MnDOT	Minnesota Department of Transportation
mV_{CSE}	mV versus copper–copper sulfate reference electrode
NaCl	sodium chloride
PC	plastic-coated
QA	quality assurance
QC	quality control
SC	stainless steel–clad
SCA	stainless steel–clad type A
SCB	stainless steel–clad type B

SCC	stainless steel–clad type C
SS	stainless steel
STDEV	standard deviation
V_{CSE}	V versus copper–copper sulfate reference electrode
WisDOT	Wisconsin Department of Transportation
WSDOT	Washington State Department of Transportation
ZC	zinc-clad

Symbols

i_{corr}	corrosion current density
I_{corr}	corrosion current
$i_{macro\text{-}cell}$	macro-cell corrosion current density
Rp	polarization resistance
$R_{coating}$	coating impedance
$t_{initiation}$	time-to-corrosion initiation
$t_{propagation}$	time-to-corrosion propagation
Z'	real component of impedance
Z"	imaginary component of impedance

CHAPTER 1. INTRODUCTION

Jointed plain concrete pavement (JPCP) uses contraction joints to control cracking and does not use any reinforcing steel. Its joint spacing is usually less than about 20 ft. On the other hand, jointed reinforced concrete pavement (JRCP) uses contraction joints and reinforcing steel to control cracking. Its transverse joint spacing varies between 25 and 50 ft, which is longer than that of JPCP. In JPCP, dowel bars are typically used at transverse joints and tie bars at longitudinal joints. Dowel bars are typically 1.25 to 1.5 inches in diameter and 18 inches in length, and they are typically spaced 12 inches apart. Transverse joint spacing is selected so that temperature and moisture stresses do not produce intermediate cracking between joints. In JRCP, dowel bars are also typically used at transverse joints, and the reinforcing steel/wire mesh contributes to load transfer across cracks. Transverse joint spacing is selected so that temperature and moisture stresses produce cracking between joints and reinforcing steel or a steel mesh is used to hold these cracked pavement components (concrete, dowel bar, mesh) together.[1,2]

A dowel bar is a load transferring device that transfers one rigid concrete pavement section to another and maintains the vertical and horizontal alignments between the two adjoining sections. It is generally inserted into the mid-depth of the section and coated with a bond breaker to let the bars move freely in the longitudinal direction (traffic direction).[3] Therefore, it can reduce movement-related distress such as pumping, faulting, and corner breaks.[4] Conversely, dowel bars can also cause pavement deterioration through corrosion caused by applied deicers penetrating into the pavement joints. The corroding dowel bars may result in the shear failure of the bar if the cross-sectional area of the bar at the joint is significantly reduced by corrosion process. The other negative effect of the dowel corrosion is the restriction of movement during pavement contraction/expansion due to the buildup of corrosion products. In both ways, corrosion of dowel bars can compromise the durability and functionality of the rigid concrete pavement. Most concrete pavement failures are centered on the material selection.[5]

To reduce the risk of corrosion, the fusion-bonded, epoxy-coated (EC) dowel bars became a commonly used corrosion protection system in lieu of the uncoated, carbon steel (CS)–dowel bars. Both materials are smooth and round to facilitate an increase in the load transfer efficiency (LTE). Like EC reinforcing steel, the epoxy coating on the dowel bar provides a physical barrier against water, chloride ions, and oxygen and also serves as an electrical insulator that can isolate the steel substrate from the surrounding environment.

In the past, the majority of the concrete pavements of the interstate highways and primary roadways in the United States were designed on the basis of a 20- to 25-yr initial low-maintenance service life.[6] As traffic congestion and lane closures due to road repairs worsened over the years, a longer initial service life of 40 yr or more became a more attractive choice of pavement design to reduce user delays. The extended service life can also reduce maintenance costs. As a result, so-called long-life pavement strategies have become popular in nearly last decade. Major characteristics of long-life pavement include an original concrete service life of 40 yr or more with minimal maintenance and repairs, no premature deterioration caused by construction and materials, and a desirable ride ability/surface texture.[6]

The use of more corrosion-resistant dowel bars in long-life pavement seems appropriate and timely in the course of technological evolvement in the area of concrete pavement design and construction. For example, the Minnesota Department of Transportation (MnDOT) specifies, in their construction specifications, corrosion-resistant dowel bar materials, including solid stainless steel (SS), stainless steel–clad (SC), SS pipe or tube, plastic-coated (PC) steel, and zinc-clad (ZC) steel.[6] The Washington State Department of Transportation (WSDOT) also requires various corrosion-resistant metallic dowel bars with different levels of protection, such as solid SS, SC, SS sleeve with an EC insert, microcomposite steel, ZC steel, and EC steel, depending on the risk of corrosion. Their specification requires smooth and round dowel bars to be 1.5 inches in diameter and 18 inches in length and installed in 12-inch spacing.[6]

Many studies have investigated the structural behaviors of various bar materials and bar geometries. Due to some concerns, in recent years, regarding the long-term performance of EC dowel bars, laboratory and field evaluations of alternative dowel bars, including fiber-reinforced polymer (FRP) bars and other corrosion-resistant metallic bars, were undertaken by a number of agencies to understand the corrosion resistance of these new materials.

As part of the same effort, an independent Federal Highway Administration laboratory study was launched to investigate the corrosion resistance of seven metallic dowel bars (with uncoated black bars as the control) in accelerated corrosion testing for 452 d followed by autopsy work. When the present study started, in 2006, the selected bar materials represented all of the metallic bar products available at that time except for a high-strength microcomposite steel. This report presents the experimental procedure, test results and data analysis, and conclusions of the study.

CHAPTER 2. LITERATURE REVIEW

The literature search found that many laboratory and field studies have evaluated the performance of various metallic and non-metallic dowel bars. However, the majority of them were focused on the structural behaviors in terms of LTE, falling weight deflection, flexural bending moment, etc. Only a few studies were directly related to the corrosion of metallic dowel bars. Reviewed studies presented little experimental data to quantify the corrosion performance of these metallic dowel bars. This chapter summarizes major literature review findings pertaining to corrosion aspects of different metallic dowel bars.

In 1999, McCallion reported the corrosion performance of EC dowel bars from a field study.[5] The EC specimens exhibited little to no bond between the epoxy coating and the steel substrate. It appeared that the coating disbondment was a result of cycling of the joint. Also, pitting corrosion and severe section loss were noted after the cores were taken from the area of the sawed portion of the joint.

The Wisconsin Department of Transportation (WisDOT) constructed a 1-mi-long test section with EC dowel bars and another 1-mi-long control section without dowel bars in 1984.[7] Immediately following the construction, a long-term field study, over 12 yr (1984 to 1996), was carried out to compare the performance of a non-reinforced concrete pavement with randomly spaced, skewed contraction joints using dowels bars with respect to the control section without dowel bars. After 5 yr of service, in 1989, eight core samples were taken at randomly selected joints in the doweled test section. WisDOT reported that none of the samples showed corrosion on the dowel bars. However, they did not point out that the lack of corrosion was probably due to insufficient chloride accumulation. Even after 12 yr in service, the EC dowel bars in the test section remained intact without corrosion. Unfortunately, WisDOT did not report final chloride concentration data at the bar depth. The long-term field study concluded that the life of the doweled pavement was estimated to last approximately 2.5 times longer than the non-doweled pavement prior to any maintenance or rehabilitation. The analyzed data indicated that a pavement without dowel bars would cost approximately 13.1 percent more than one with dowel bars over a 25-yr service life.

The same highway agency also realized that the corrosion resistance of EC dowel bars can be compromised if the epoxy coating is damaged during installation or load transferring; subsequently, corrosion can start at the damaged areas. As a result, WisDOT awarded a paper study in 2003 to seek information regarding alternative materials, such as FRP, solid SS, and SC bars. From this initiative, eight past and ongoing studies were identified, and a brief description of each study was given in a referenced report.[8] Some of the identified studies are described in the following section.

Researchers at Iowa State University identified 21 topics pertaining to dowel bar research that had the most significant knowledge gaps.[9] One of them was the acceptable corrosion of steel dowel bars. The researchers pointed out that an EC dowel bar is susceptible to corrosion caused by moisture during the concrete curing process and coating damage occurring during the manufacturing, transportation, and placement at the job site. They recommended determining an

acceptable level of steel corrosion before the EC bar became useless, became inadequate, or caused joint lock-up.

Historically, MnDOT had used 18-inch-long plain steel–dowel bars prior to the exclusive use of the 15-inch-long EC dowel bars in accordance with American Association of State and Highway Transportation Officials' (AASHTO) M284.[10] By 2002, EC dowel bars had been used in Minnesota for just over 20 yr.[11] Many EC dowel bars have not shown deterioration, but some bars extracted during the repair projects have exhibited severe corrosion and necking. Corrosion-resistant dowel bars were included in their high-performance concrete (HPC) specification. In 2003, MnDOT published their experience regarding the development and implementation of the specification.[11]

They specified four different dowel bars (bid price per bar): 1.5-inch EC bar ($5.20), 1.5-inch solid SS bar ($19.70), 1.5-inch SC bar ($11.60), and 1.75-inch SC bar ($14.30). All SS dowel bars used in Minnesota have been specified to meet the elevated corrosion resistant requirements of grade 316L. Of the 41,625 dowels needed for the pilot project, 36,650 bars (88 percent) were to be the 1.5-inch SC bars. The other bar types were also included for comparison purposes. The use of the SC bars created some issues later due to their limited availability. So, MnDOT had to substitute it with two SS bar types despite the cost overrun. The annualized cost for a 60-yr design using solid SS dowel bars was significantly higher than that of a standard 35-yr design without user-cost considerations.[11] Due to increased cost and short supply of the 1.5-inch SC corrosion-resistant dowel bars, implementation became an issue.

Larson and Smith reported alternative dowel bars and their price ranges.[12] The cited price information is comparable to that given in the preceding MnDOT paper.[11] The authors also mentioned several emerging bar materials, including a microcomposite steel (MMFX 2) dowel bar, solid SS lean duplex SS (LDX 2101) dowel bar, and ZC dowel bar. The following key information about the price and description of individual dowel bars was extracted from the report:

- PC dowel bar ($3 to $6).
- Solid SS dowel bar ($18 to $20).
- SC dowel bar ($6 to $11).
- SS tube filled with cement grout ($5 to $10).
- FRP composite dowel bar ($4 to $9).
- FRP composite tube filled with cement grout ($4 to $9).
- EC dowel bar ($2.50 to $5).

PC DOWEL BAR

The plastic coating material was a 20- to 30-mil-thick polyethylene that conformed to AASHTO M254, type A.[13] A thin mastic coating can be installed between the substrate and the plastic coating. The original coating was developed to protect underground pipelines from corrosion in the 1960s. This coated bar is comparable to that of the EC bar, but no bond breaker is required, which can be a benefit during installation.

SOLID SS DOWEL BAR

For the most common solid SS dowel bars, types 316 and 316L have been used because they are high-strength austenitic SS and also highly corrosion resistant. However, their initial cost was about five times the cost of the EC bars. Considering lifecycle costs, these high-end materials are more economical than the EC bar thanks to a much longer service life.[12] Type 304 SS is less corrosion resistant compared with 316 grades.

SC DOWEL BARS

For the most popular SS cladding material, types 316L and 316 have been used. Typical clad thickness varies between 7 and 9 mil. As opposed to the EC bars, SC bars have a strong bond between the cladding layer and the CS core, and no damage can be done during the construction process.

SS TUBE FILLED WITH CEMENT GROUT

This bar type utilizes the same highly corrosion-resistant type 316L SS in the form of a tube that is filled with a high-strength cementitious grout material. It is reported that preventing the formation of grout voids when filling the tube with grout can be difficult. This type of dowel bar is intended to provide high corrosion resistance of solid SS or SC bars at a much lower cost while meeting the requirements of sufficient stiffness and structural integrity under loading.

Larson and Smith also published another final report in 2011 based on a pooled fund study.[4] According their analysis, the life of the epoxy coating on mild CS dowel bars evaluated in Ohio and Wisconsin appeared to be in the range of 25 to 30 yr. A significant number of the EC dowel bars experienced coating disbondment. The exposed steel substrate exhibited corrosion products and pits without significant section loss in most cases. The observed EC bar degradation was linked to the initial coating quality and coating damage that occurred during installation. The authors reported that the extracted EC bars in Wisconsin tended to show more section loss than those in Ohio. Also, an apparent correlation between chloride concentration at the bar depth and extent of corrosion was not observed in either State. The authors concluded that the use of the EC bar seemed to be adequate for 30-yr design life pavements but should not be considered for 50-yr design life pavements, where excessive section loss is anticipated in corrosive service environments. In addition, they discussed two older projects in Ohio constructed with PC dowel bars. The extracted PC dowel bars were in excellent condition after 33 yr in service, and the overall pavement condition of these projects was very good, with little visible joint deterioration. The PC dowel bars with limited coating delamination were reported to be more durable and less susceptible to damage during handling and construction than the EC bars. The authors attributed the PC dowel bars' good corrosion resistance to the intermediate mastic coating between the plastic coating and the steel substrate. However, the Michigan Department of Transportation reported that the PC dowel bars showed excellent performance for the first 10 yr but exhibited coating disbondment after 30 yr.[12] In comparison, the EC bars maintained their pristine condition, leading to exclusive use of the EC bars in the State.[12]

Snyder published test results of the accelerated corrosion testing of the ZC dowel bars.[14] These relatively new bars are produced by mechanically bonding a 50-mil-thick layer of solid zinc

alloy strip to a standard 1.5-inch-diameter CS bar that conforms to ASTM A615.[15] The author claimed that the thickness of the zinc alloy cladding was designed to provide about 100 yr of cathodic protection in the 5-percent salt environment. The zinc cladding offers a physical barrier to the CS core and also cathodic protection of exposed steel by sacrificial action of the zinc alloy. Corrosion resistance of the ZC dowel bars ($9 per bar) were evaluated for 12 weeks in 5-percent sodium chloride aqueous solution along with four different types of dowel bars: an uncoated CS dowel bar (not reported), an EC dowel bar (<$5 per bar), a 316L SC dowel bar ($12 per bar), and a microcomposite dowel bar (not reported). Four holes were drilled in each of the barrier-coated bar types to simulate accidental damage. Additional specimens were prepared with slotted ZC dowel bars to determine the effectiveness of cathodic protection. Corrosion performance of each bar material was monitored with progressive changes of appearance on the bar samples, and the loss of iron was estimated with atomic absorption spectroscopy to calculate the corrosion rate of each material. The author presented the test results: the corrosion rates of the EC dowel bars and the SC dowel bars were 40 to 90 times and 250 to 500 times higher than those of the ZC dowel bars, respectively, due to a mild cathodic protection of the ZC dowel bars, and the ZC dowel bars were effective in preventing corrosion of the CS core through cathodic protection, even with the artificial damage. The author concluded that the ZC and the SC dowel bars are suitable for long-life HPC pavements, and the ZC dowel bars were unlikely to experience too much corrosion at the joints to reduce the LTE.

WisDOT initiated a 5-yr field study involving a 9-inch-thick, 833-ft-long test section containing microcomposite steel–dowel bars as part of JPCP new construction in 2002.[16] This study was to determine if the in-service use of microcomposite steel–dowel bars resulted in better pavement performance compared with the EC bar case. This material conforms to ASTM A1035 with a minimum tensile strength of 150 ksi and a minimum yield strength of 100 ksi.[17] Corrosion performance, one of the test variables, was judged by corrosion morphologies of the extracted dowel samples from the field cores taken 5 yr after construction. Cost effectiveness and construction issues were also evaluated. The JPCP test sections constructed with both types of dowels performed equally well after 5 yr. The field cores cut through dowel bars revealed no corrosion on both bar types. The author did not report chloride concentrations at the bar depth. The initial cost per two-lane project mile was calculated. While both the EC and microcomposite bars provided superior performance, the cost of the microcomposite dowel bar section was 32 percent higher than that of its EC bar counterpart. Based on the inconclusive results of the field study, inconsistent corrosion test results reported in the literature, and the higher initial cost, the author did not recommend that the microcomposite bars be approved for use in future WisDOT JPCP construction.

Mancio et al. evaluated seven types of 1.5-inch steel dowel bars in three phases.[18] Phase I and phase II studies were conducted in the laboratory using small-scale concrete beams. The phase III study was also carried out in the laboratory using three concrete pavement slabs that were extracted from a dowel bar retrofit project in Washington State. The bars employed in phases I and II included the following:

- CS dowel bar—phases I and II.
- SC dowel bar—phases I and II.
- SS tube filled with grout—phases I and II.
- Microcomposite steel dowel bar—phase II.

- Flexible EC dowel bar (green color coating, designation ASTM A775)—phase II.[1](19)
- Non-flexible EC dowel bar (purple color coating, ASTM A934)—phase II.(20)
- Non-flexible EC dowel bar (gray color coating, ASTM A934)—phase II.(20)

The SC bars had a CS core covered with an approximately 20-mil-thick SS cladding. The SS tubes had a wall thickness of approximately 20 mil and were filled with a cementitious grout. Every EC bar examined for holidays had one or more defects on the coating, especially along the edges at the ends. The ends of the SC and EC bars were protected with coatings. Other material characteristics, including types of SS, were not presented in the report.

Half-cell potentials were measured to determine the probability of corrosion activity of the steel according to ASTM C876.(21) The linear polarization resistance (LPR) technique is a well-established method to determine the rate of corrosion, which can be expressed in terms of the corrosion current density and is inversely proportional to the polarization resistance. Laboratory investigations using scanning electron microscopy were also carried out in phase II to evaluate the corrosion performance of the dowel bars. Chloride analyses were performed on concrete cores extracted from different types of concrete beams and pavement slabs.

At the end of phase I testing of concrete beams with joints, the researchers observed that uncoated CS dowel bars had the shortest corrosion initiation period, and the EC dowel bars performed far better with a significantly extended corrosion initiation period. The SS tubes and SC dowel bars provided the highest resistance to the onset of corrosion. After 6 mo of cyclic ponding, visual examination revealed that the CS dowel bars exhibited uniform corrosion along the bar and the EC dowel bars had localized corrosion at defects. No visible corrosion was observed on both types of SS based dowel bars.

In phase II testing of concrete beams with joints, the EC dowel bars showed localized corrosion at defective areas (e.g., pinholes, voids). No significant difference was observed on the performance of non-flexible and flexible EC dowel bars. Based on LPR and corrosion current density data, the researchers verified that the CS dowel bars were expected to have the fastest rate of corrosion propagation among the bar materials included in this study. The microcomposite steel–dowel bars exhibited approximately 35 times higher polarization resistance and moderate corrosion rates compared to the CS dowel bars. Both SC and SS tube dowel bars exhibited the highest corrosion resistance, with 73 times greater polarization resistance and lower corrosion than the CS dowel bars. Visual inspections of the tested dowels revealed heavy and mostly uniform corrosion on the CS dowel bars, light corrosion on the microcomposite steel–dowel bars, and no visible corrosion on the SC and SS tube dowel bars. Statistical analyses of the results confirmed that dowel bar type had a statistically significant effect on the quantitative parameters studied (i.e., half-cell potential, polarization resistance, and corrosion current density).

At the end of the phase III study, the cores taken at the joints of the extracted pavement slabs showed a considerable amount of corrosion products beneath the epoxy coating. The researchers speculated that corrosion was likely to have contributed to the loss of the LTE of the joint in the

[1]In 2012, a separate ASTM standard became available for EC dowel bars.(22)

presence of low-strength corrosion products at the interface between the concrete and the dowel bar. Half-cell potential and LPR data matched the visual observations of active corrosion.

As expected, chloride concentrations close to the field joints were significantly higher than in other regions of the pavement. This was because chloride ions that migrated through the open joint had easier access to the dowel bars. Such a condition led to higher, localized chloride concentrations beneath the joint. The chloride concentrations were more constant along the depth profile in the laboratory cores compared with those of field cores. The field cores taken from five out of six projects exceeded the chloride threshold for the CS dowel bars. Thanks to accelerated laboratory corrosion experiments using a 3.5-percent sodium chloride (NaCl) solution, corrosion could be observed in nearly all samples with 18 mo of exposure. The researchers suggested that the actual field conditions and local environment should be taken into account when choosing the appropriate material for a given project.

At the end, the researchers made the following recommendations:

- The uncoated CS dowel bars should not be used.
- The EC dowel bars present some risk of corrosion, primarily localized corrosion at holidays and the ends of the bars. Therefore, quality control (QC) checks should be implemented to control holidays, bar ends should be coated with epoxy coating, and care must be taken with the EC dowel bars during shipping, storage, and installation.
- The use of SC, SS tube, or microcomposite steel–dowel bars should be considered for locations with a high risk of elevated chloride exposure. The selection of a specific corrosion-resistant dowel bar should be based on further field investigations and cost analysis.
- A field study is recommended at several mountain pass locations to measure the chloride content of snowmelt after sand/salt application for comparison with various chloride concentration data reported in the laboratory study. The results of this study should also be used to further refine the risk assessment in the critical locations.

WSDOT published a technical report that discussed various aspects of dowel applications for new and existing concrete pavement.[(23)] The covered topics included an introduction to alternative dowel bars, dowel bar selection protocol, and cost versus corrosion resistance of the dowel bar types. WSDOT ranked corrosion resistance of the different metallic dowel bar types from the highest to the lowest as follows:

1. Solid SS bar ($30 to $40; average $35).
2. SC bar ($17 to $20; average $19).
3. SC over EC bar (no data).
4. Microcomposite steel bar ($9 to $24; average $14).
5. ZC bar ($13, based on a single project).
6. EC bar (ASTM A934, $8 to $12; average $10).[20]

It can be seen that level of corrosion resistance and cost are reasonably related to each other. This 2013 document indicated that WSDOT was not using SS types due to the high cost and unavailability of SC bars.[23]

Table 1 summarizes the price information of various metallic dowel bars presented previously. These bar prices pertain to 1.5-inch dowel bars only. It can be easily seen in table 1 that dowel bar prices varied significantly over 11 yr because they depended on many factors, such as the regional markets, year, and fluctuating prices of precious metals needed for SS alloys.

Table 1. Price comparison chart of metallic dowel bar materials reported in the literature.

Materials	Larson and Smith (2002)[12]		Turgeon (2003)[11]		Snyder (2005)[14]		WSDOT (2013)[23]	
Bar type	Average price	Ratio to EC	Average price	Ratio to EC	Average price	Ratio to EC	Average price	Ratio to EC
EC	$3.75	1.0	$5.20	1.0	$5.00	1.0	$10.00	1.0
Solid SS	$19.00	5.1	$19.70	3.8	—	—	$35.00	3.5
SC	$8.50	2.3	$11.60	2.2	$12.00 (type 316L)	2.4	$19.00	1.9
SS tube filled with grout	$7.50	2.0	—	—	—	—	—	—
ZC	—	—	—	—	$9.00	1.8	$13.00	1.3
PC	$4.50	1.2	—	—	—	—	—	—
Microcomposite steel	—	—	—	—	—	—	$14.00	1.4

—Not applicable.

It was difficult to develop a uniform price index for each material based on limited and possibly biased price information. Instead, calculating relative ratios of individual bar prices with respect to the EC dowel bar price (as the base material) in the same literature seems to be a reasonable approach to understand their price competitiveness. The EC and the solid SS dowel bars are two cost extremes, and the others fall between these upper and lower limits. It should be noted that SC dowel bars are the best choice of material when corrosion resistance and cost are considered together.

Based on only a few studies directly related to the corrosion of metallic dowel bars in the literature search, all the reported data suggest that uncoated CS dowel bars should not be used because they are the least corrosion resistant. EC dowel bars, the most commonly used materials other than uncoated CS dowel bars, demonstrated mixed performance in the field; while they

could remain intact without corrosion after 12 yr, some extracted samples exhibited severe deterioration in terms of coating disbondment, pits without significant section loss, and even necking. The corrosion resistance of EC dowel bars can be compromised when the epoxy coating is damaged during installation or load transferring, and subsequent corrosion can start at the damaged areas. In order to increase its corrosion resistance, QC checks should be implemented to control holidays, protect bar ends with epoxy coating, and exercise caution during shipping, storage, and installation.

For other types of dowel bar materials, the level of corrosion resistance and cost are reasonably related to each other. EC and solid SS dowel bars are two cost extremes, and the others fall between these upper and lower limits. The initial cost of the latter can be as high as five times that of the former. However, when considering lifecycle costs, types 316 and 316L based materials are more economical than the EC bars because they should provide a much longer service life due to their elevated chloride threshold values. Among the former, SC dowel bars were the best choice of material until implementation became an issue due to their increased cost and short supply (currently, none of them are available in the market). Other types, such as microcomposite and ZC dowel bars, still do not seem to be attractive corrosion-resistant alternatives due to their high costs and sparse or questionable positive performance data.

CHAPTER 3. EXPERIMENTAL PROCEDURE

CHARACTERISTICS OF TESTED DOWEL BARS

A total of eight metallic dowel bar materials were chosen for this study as follows:

1. Uncoated CS (black) bar.
2. EC bar.
3. Hot-dip galvanized (HDG) bar.
4. ZC bar.
5. Stainless steel–clad type A (SCA) bar.
6. Stainless steel–clad type B (SCB) bar.
7. Stainless steel–clad type C (SCC) bar.
8. Type 316L solid SS bar.

At least six bar samples were acquired per bar type through bar manufacturers and a national steel distributor. Each bar sample was 1.5 inches in diameter and 12 inches long. All bar materials, except for black and solid SS bars, had one or two outer protective layers in the form of coating, SS cladding, or both. The black dowel bar conformed to ASTM A615, and it served as a control and represented the least corrosion-resistant material in this study.[15] The solid SS dowel bar was type 316L, which served as the other control and possessed the highest corrosion resistance in this study. The fusion-bonded EC dowel bar confirmed to ASTM A775 with an average coating thickness of 10.2 mil.[19] Some EC dowel bars contained a small number of as-received coating defects. HDG and ZC bars had a sacrificial layer of zinc on them. The HDG dowel bar conforming to ASTM A767 possessed a pure zinc layer with an average thickness of 4.2 mil.[24] The ZC dowel bar was produced by mechanically bonding a 47-mil-thick pure zinc strip around the ASTM A615 dowel.[15] Figure 1 shows a cross-sectional view of the ZC bar. A localized small gap can be seen along the zinc-cladding/core interface.

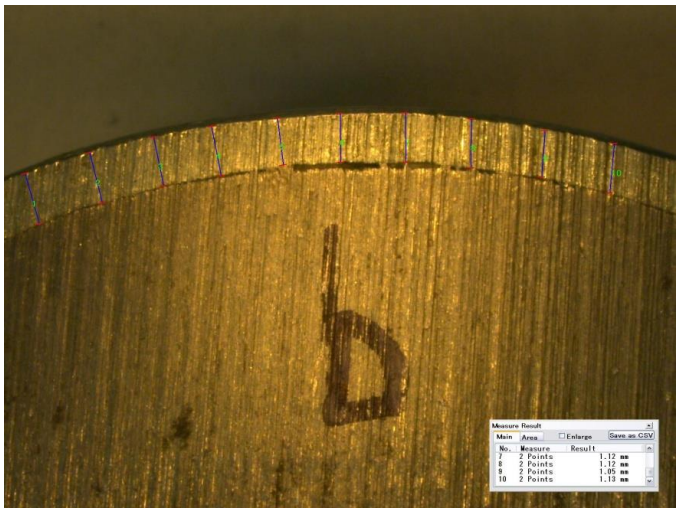

Source: FHWA.

Figure 1. Photo. Photomicrograph of a ZC bar with 45- to 48-mil-thick cladding.

Three types of SC dowel bars were employed in this study. Their cross-sections are shown in figure 2. The SCA dowel bar had a type 316 SS-cladding layer of 46 mil. The SCB dowel bar also had a type 316 SS-cladding layer with an average thickness of 84 mil. As shown in figure 2, its cladding thickness was not uniform. The SCC dowel bar had a dual protective system of a 64-mil-thick type 316L SS cladding and a 17-mil-thick fusion-bonded epoxy coating applied on the ASTM A615 CS dowel bar.[15] Its magnified cross-section view is shown in figure 3. Table 2 and table 3 summarize the thicknesses of protective layers in terms of mean, standard deviation (STDEV), and coefficient of variation (CV) before and after corrosion testing was terminated, respectively.

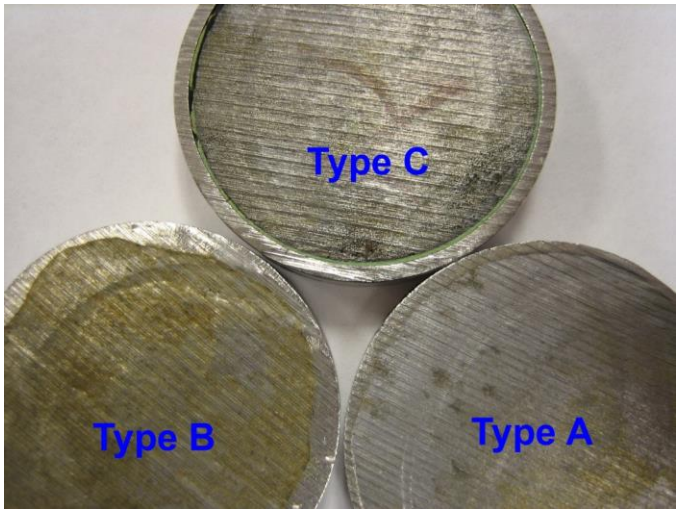

Source: FHWA.

Figure 2. Photo. Cross-sectional view of three types of SC bars.

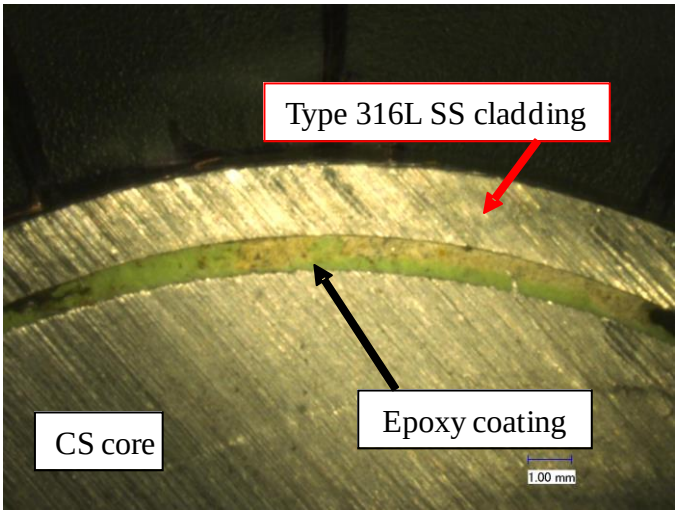

Source: FHWA.
1.00 mm = 0.04 inches.

Figure 3. Photo. Photomicrograph of an SCC bar.

Table 2. Baseline protective layer thickness.

Bar Type	Mean (mil)	STDEV (mil)	CV (%)
EC	10.2	2.0	19.9
HDG	4.2	0.4	9.8
ZC	46.9	3.1	6.7
SCA	45.1	14.1	31.2
SCB	88.9	24.0	27.0
SCC cladding	63.6	2.8	4.5
SCC epoxy coating	16.6	5.2	31.4

Table 3. Final protective layer thickness.

Bar Type	Mean (mil)	Maximum (mil)	Minimum (mil)	STDEV (mil)	CV (%)
HDG	2.5	3.6	0.7	0.8	31.8
ZC	31.5	49.2	5.1	10.1	31.9

When the bars were delivered, there were no records regarding pickling treatment of the solid SS and SC dowel bars. Numerous scratches and some isolated rust spots were already visible on most of the SC dowel bars upon arrival.

PRE-CONDITIONING OF DOWEL BARS PRIOR TO EMBEDMENT IN CONCRETE

Artificial defects were introduced into the bar types that had external protective layers, which included EC, HDG, ZC, and all three types of SC dowel bars. For each slab containing these bar types, two bars contained three equally spaced 0.375-inch diameter holes (0.590-percent damage versus total surface area), and another two bars contained three equally spaced 0.125-inch diameter holes (0.070-percent damage versus total surface area). Figure 4 shows two HDG bars containing each defect size. The remaining two bars were without intentional defects. Table 4 summarizes individual bar conditions in each slab in terms of relative position within the slab, defect size, bar type, and use of bond breaker.

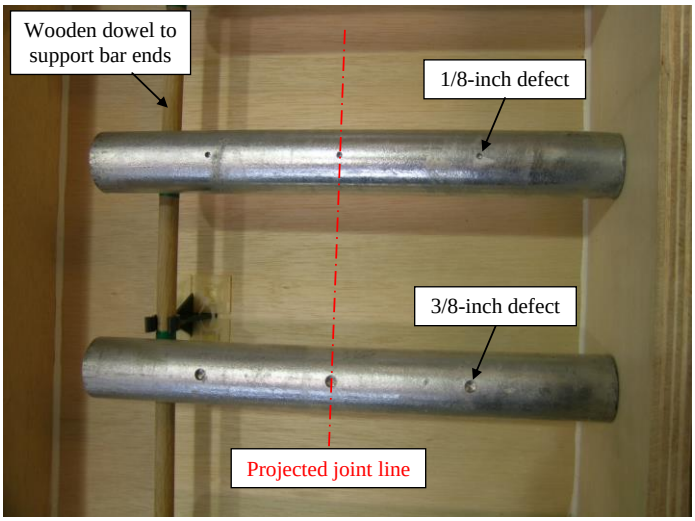

Source: FHWA.

Figure 4. Photo. Two defect sizes.

Table 4. Test slab information.

Slab No.	Slab ID	Condition	L1*	L2*	L3*	Center*	R3*	R2*	R1*	Use of Bond Breaker
1	Black (CS)	Material	CS	CS	CS	SS 316L	CS	CS	CS	Yes
1	Black (CS)	Defect size (%)	—	—	—	—	—	—	—	Yes
2	EC	Material	EC	EC	EC	SS 316L	EC	EC	EC	Yes
2	EC	Defect size (%)	0.00	0.59	0.07	0.00	0.59	0.07	0.00	Yes
3	HDG	Material	HDG	HDG	HDG	SS 316L	HDG	HDG	HDG	Yes
3	HDG	Defect size (%)	0.00	0.59	0.07	0.00	0.59	0.07	0.00	Yes
4	ZC	Material	ZC	ZC	ZC	SS 316L	ZC	ZC	ZC	Yes
4	ZC	Defect size (%)	0.00	0.59	0.07	0.00	0.59	0.07	0.00	Yes
5	SCA and SCB	Material	SCA	SCA	SCA	SS 316L	SCB	SCB	SCB	Yes
5	SCA and SCB	Defect size (%)	0.00	0.59	0.07	0.00	0.07	0.59	0.00	Yes
6	SCC	Material	SCC	SCC	SCC	CS	SCC	SCC	SCC	Yes
6	SCC	Defect size (%)	0.00	0.59	0.07	0.00	0.59	0.07	0.00	Yes
7	Assorted	Material	EC	ZC	SCA	SCC	HDG	SCB	CS	No
7	Assorted	Defect size (%)	0.00	0.00	0.00	0.00	0.00	0.00	0.00	No

*Bar identification and bar type.
—None.

FABRICATION OF CONCRETE TEST SLABS

As summarized in table 4, seven concrete slabs were made for this study. The overall dimensions of each slab were 36 inches wide by 15 inches long by 5.5 inches thick, and each slab contained an artificial transverse pavement joint and seven dowel bars spaced 5 inches apart beneath the joint to simulate a JPCP. Figure 5 through figure 7 show details of the slabs.

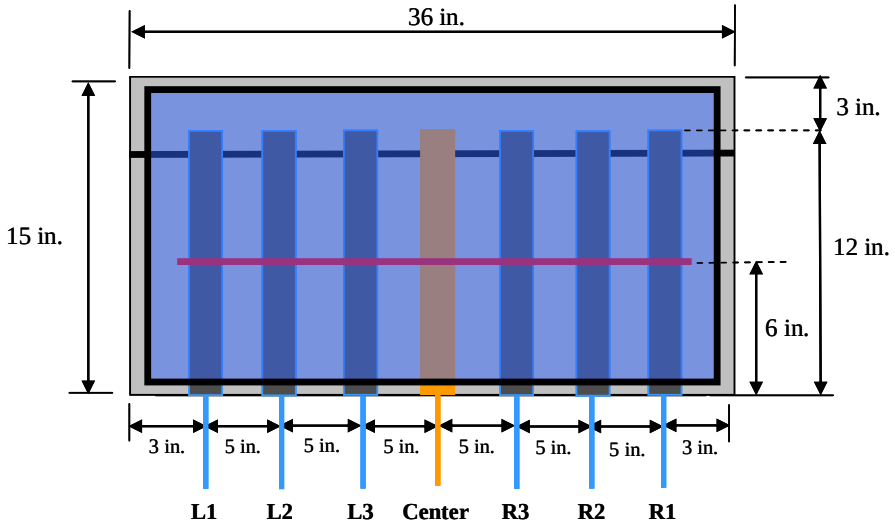

Source: FHWA.
Note: in. = inches.

Figure 5. Illustration. Schematic of slab specimen (not to scale)—plan.

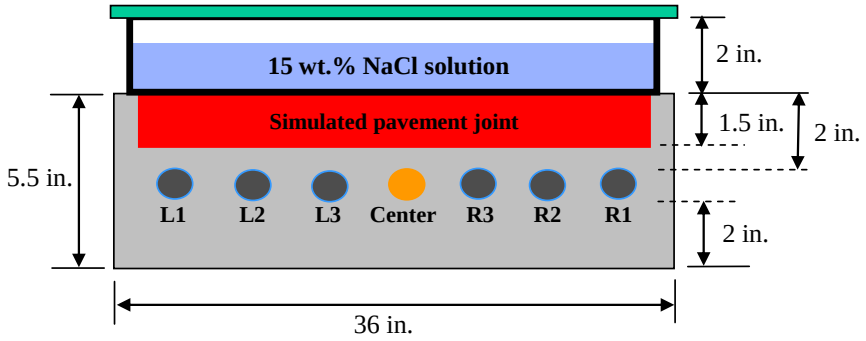

Source: FHWA.
Note: in. = inches; wt. % = weight percent.

Figure 6. Illustration. Schematic of slab specimen (not to scale)—elevation.

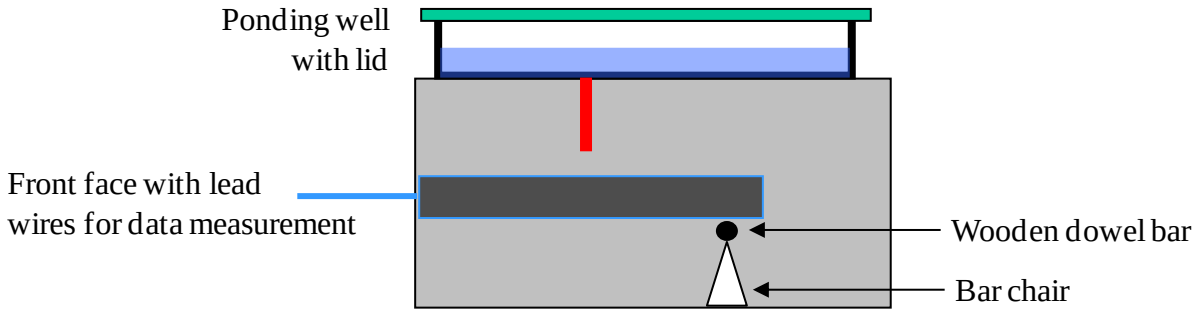

Source: FHWA.

Figure 7. Illustration. Schematic of slab specimen (not to scale)—profile.

The simulated pavement joint was created by placing a 0.25-inch-thick and 2-inch-deep plastic shim across the mold. The artificial joint reached 1.5 inches deep into the concrete so that an undisturbed concrete cover measured 0.5 inches thick beneath the joint and 2 inches thick elsewhere. The bars were placed in a way that one end (with a tapped hole for electrical connection) of each bar was exposed to the slab's front face and electrical connections, which were made using a set of SS screws, washers, and a piece of solid copper wire, as shown in figure 7. The other end of the bars rested on a 0.5-inch-diameter wooden dowel. These bare ends were not protected with coatings or plastic caps. For each bar containing three artificial defects, the middle one was always situated beneath a simulated pavement joint, as shown in figure 4, regardless of defect size.

When a bar such as a SS one possesses high corrosion resistance or it corrodes at a negligible rate due to a passive film formed in the highly alkaline environment of concrete, its corrosion potential remains relatively unchanged. If the bar corrodes in the presence of excessive chloride ions or concrete carbonation, its corrosion potential is more negative than its non-corroding potential. As soon as an electrical connection is made between the corroding bar and non-corroding one, macro-cell corrosion (a form of galvanic corrosion) current starts to flow under a potential difference developed between the two bars: the larger the potential difference, the higher the macro-cell corrosion current. The corroding bar with the more negative corrosion potential becomes the macro-anode, and the non-corroding one with the more positive corrosion potential serves as the macro-cathode. Historically, a common evaluation technique for corrosion resistance of metals in concrete is to measure the macro-cell corrosion current.

In this study, each concrete slab contained at least two bar types to create macro-cell corrosion between the dissimilar bars. Table 4 lists individual bar types according to relative position in each slab. For slab 1 through slab 5, a type 316L solid SS bar, the most corrosion-resistant material employed in this study, was placed in the center of the mold as a single macro-cathode, and a group of three bars was positioned on both sides of the SS bar to serve as six independent macro-anodes. The actual conditions of these slabs are shown in figure 8 through figure 12. Slab 6 had a black bar in the center position and six SCC bars in other positions, as shown in figure 13. A black bar was substituted for a type 316L solid SS bar because there were no more solid SS bars available. In such a bar arrangement, the black bar still acted as a single macro-anode and the SCC bars as six separate macro-cathodes thanks to its highly corrosion-resistant type 316 SS cladding. Slab 7 contained all seven bar types excluding a type 316L solid SS bar. An SCC

bar was placed in the center to serve as the macro-cathode. Figure 14 shows the bar arrangement in the assorted slab. These bars did not have any artificial defects and were not coated with a bond breaker. A commercially available bond breaker was applied on the bars embedded in slab 1 through slab 6 to emulate actual practices in the field.

Source: FHWA.

Figure 8. Photo. Black bars and a type 316L solid SS bar in the center (black bar slab).

Source: FHWA.

Figure 9. Photo. EC bars and a type 316L solid SS bar in the center (EC bar slab).

Source: FHWA.

Figure 10. Photo. HDG bars and a type 316L solid SS bar in the center (HDG bar slab).

Source: FHWA.

Figure 11. Photo. ZC bars and a type 316L solid SS bar in the center (ZC bar slab).

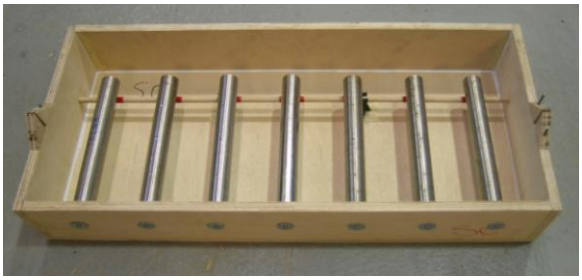

Source: FHWA.

Figure 12. Photo. SCA and SCB bars and a type 316L solid SS bar in the center (SCA and SCB bar slab).

Source: FHWA.

Figure 13. Photo. SCC bars and a black bar in the center (SCC bar slab).

Source: FHWA.

Figure 14. Photo. Assorted bar slab.

Figure 15 and figure 16 show concrete casting work in progress and fresh concrete slabs, respectively. The latter also shows plastic shims used for simulated pavement joints. A lean

concrete mix was used with a target water–cement ratio of 0.5 without any admixtures. The poor-quality concrete was designed to promote fast chloride ingress, leading to rapid corrosion initiation. The molds and plastic shims were removed after 24 h, moisture cured for 7 d, and then air-dried for 21 d in the laboratory.

Source: FHWA.

Figure 15. Photo. Casting of concrete slabs.

Source: FHWA.

Figure 16. Photo. Completed concrete slabs.

ACCELERATED CORROSION TESTING

After the 28-d curing, the concrete slabs were fitted with electrical lead wires and plastic ponding wells, as shown in figure 17. Exterior lateral faces were covered with a clear epoxy-based coating. An accelerated laboratory corrosion testing scheme was employed for 452 d. During the testing duration, the following weekly exposure cycle was repeated:

- 4-d wetting in a 15 weight percent NaCl solution at 75 °F.
- 3-d drying at 100 °F.

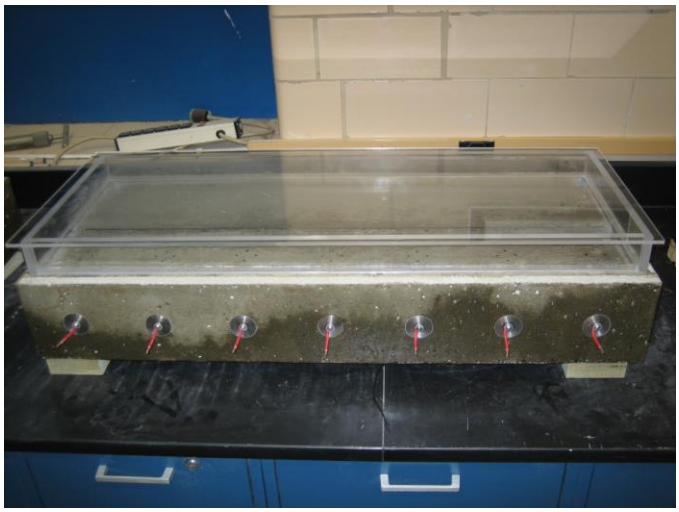

Source: FHWA.

Figure 17. Photo. A test slab with a ponding well/lid and electrical lead wires.

The salt solution was chosen to represent a high-level chloride contamination occurring on inland bridge structures and pavements from deicing salt applications. Figure 18 shows an overview of the accelerated laboratory test arrangement in a wetting cycle. The small concrete specimens shown in the photograph were for another corrosion study. During the drying cycles, the heat tent equipped with an electrical heater was closed, and the slabs were dried at the preset temperature regulated by a built-in thermostat.

Source: FHWA.

Figure 18. Photo. Exposure test setup in a heat tent.

DATA COLLECTION

The experimental data of corrosion potential, macro-cell corrosion current, and alternating current (AC) resistance were measured on a weekly basis with some exceptions. During the exposure testing, the bars in each slab were not electrically connected except for the moments when macro-cell corrosion current was measured. At the completion of each wetting cycle, these data were collected immediately after the salt solution was vacuumed off the ponding wells while the concrete surface was still wet. Figure 19 shows a photograph of an electrochemical testing in progress. In addition, instantaneous rates of corrosion were measured three times: an initial data collection and two data collections toward the end of the testing program. The following section discusses the test methods employed in this study.

Source: FHWA.

Figure 19. Photo. Electrochemical testing.

Corrosion (Half Cell or Open Circuit) Potential Measurement

The corrosion potential indicates thermodynamic corrosion tendency of steel according to ASTM C876 *Standard Test Method for Half-Cell Potentials of Uncoated Reinforcing Steel in Concrete*.[(21)] The potential data can be interpreted using the numeric magnitude technique specified in C876, appendix X1. According to the criteria, if potentials over an area are more positive than –0.200 V versus copper–copper sulfate reference electrode (V_{CSE}), there is a greater than 90-percent probability that no reinforcing steel corrosion is occurring in that area at the time of the measurement. If potentials over an area are more negative than –0.350 V_{CSE}, there is a greater than 90-percent probability that reinforcing steel corrosion is occurring in that area at the time of the measurement. If potentials are between –0.200 and –0.350 V_{CSE}, corrosion activity of the reinforcing steel in that area is uncertain. However, many factors, such as concrete resistivity, temperature, depth of carbonation, oxygen content, presence of coating, and the degree of water saturation in the concrete, can influence the potential readings.

Macro-Cell Corrosion Current Measurement

The macro-cell corrosion current was explained in the previous section. It was measured using a sophisticated commercial ammeter, which has a capability of measuring pico-ampere (10^{-12} A) level direct current. The ammeter was inserted in the electrical circuit so that positive current coming out of the macro-anode was always measured. Consecutive current measurements were made by changing the electrical connection one by one for each of six macro-anodes while maintaining the electrical connection at the macro-cathode. During the data analysis, the collected macro-cell corrosion current was converted into macro-cell current density ($i_{macro\text{-}cell}$, $\mu A/cm^2$) by dividing the current by the dowel's total surface area (365 cm^2) (note that 1 $\mu A/cm^2$ = 6.45 $\mu A/inch^2$). Then, the $i_{macro\text{-}cell}$ data were analyzed in terms of artificial defect size, bar type, and overall means.

AC Resistance Measurement

The AC resistance is measured using a commercially available soil resistance meter. The resistance data can be useful in estimating the ease of corrosion occurrence: the lower the electrical resistance, the higher the corrosion current. Originally, this instrument was developed to measure electrical resistance in soil using the Wenner 4-pin configuration. To adapt this technique for resistance measurements between two dowel bars using the Wenner 2-pin method, the center bar was connected to one terminal of the meter, and one of the six bars was connected to the other terminal of the meter. By changing wire connection one at a time, individual electrical resistances between the center bar and the six bars were measured.

Instantaneous Rate of Corrosion Measurement

Corrosion rate is a kinetic property indicating how fast corrosion is occurring at the time of measurement. In this study, the three-electrode LPR method was employed to determine the instantaneous rate of corrosion of the tested bars by means of an advanced electrochemical test instrument. For each test cell, a dowel bar served as a working electrode, and a 12-inch-long strip of type 316 SS wire mesh placed on top of the concrete surface above the working electrode was the counter electrode. A portable silver–silver chloride reference electrode was used to monitor potential during the LPR experiment. The corrosion rate measurements were made three times at 16, 402, and 452 d during the wetting cycles, as shown in figure 20. The first set of corrosion rate data collected was treated as baseline data before initiating corrosion, and the last two datasets were treated as the final corrosion rates of individual bar types.

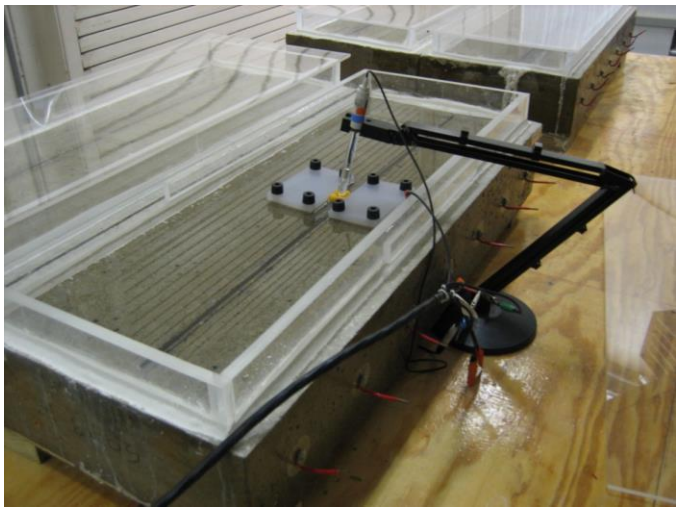

Source: FHWA.

Figure 20. Photo. Corrosion rate measurement setup.

An LPR measurement of a dowel bar applied incremental potentials to a test cell from –15 mV to +15 mV with respect to the bar's corrosion potential at a scan rate of 0.5 mV/s and a sampling period of 2 s. The corresponding current data generated in response to each polarization step were recorded by the instrument, and then, a slope of the linear region between the potential data and the matching current data was determined. By Ohm's law, this slope is called the polarization resistance (*Rp*). The experimentally determined *Rp* is used in the Stern–Geary equation to calculate the corrosion current (I_{corr}, µA) or corrosion current density (i_{corr}, µA/cm^2, dividing I_{corr} by electrode surface area). Figure 21 illustrates the LPR method. Faraday's Law calculates the mass loss at the time of measurement in terms of uniform penetration rate. In this report, all corrosion rates are reported with one of the most common units, mil per yr (mil/yr).

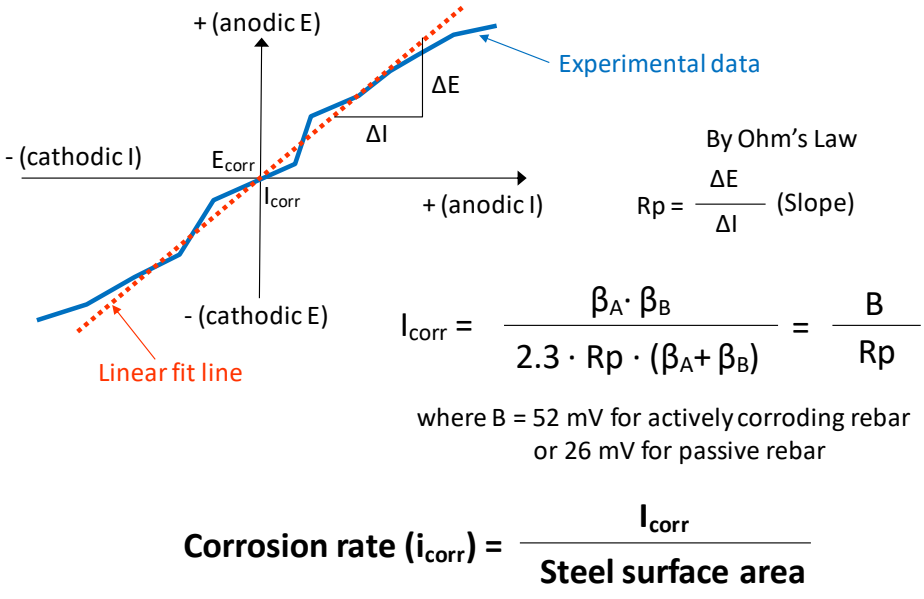

Source: FHWA.

Figure 21. Illustration. Corrosion rate determined by LPR method.

For two EC bars without intentional defects, the LPR technique did not work because its small direct current could not penetrate high-quality epoxy coating to reach the underlying steel. In such cases, the electrochemical impedance spectroscopy (EIS) technique, an alternative method to obtain *Rp*, was used. EIS employs a small AC signal to penetrate the coating. In this study, a 50 mV AC voltage was applied to the test cell from 300 kHz to 10 mHz. After obtaining the EIS data, an equivalent circuit model for coated steel was employed to fit the EIS data and estimate an *Rp* value of the steel substrate. From this, i_{corr} was calculated. Figure 22 illustrates how the EIS curve fitting work was done. The diameter of the first and the second semicircles in the Nyquist plot (real component of impedance (Z') versus imaginary component of impedance (Z") plot) represent the coating impedance ($R_{coating}$) and *Rp*, respectively.

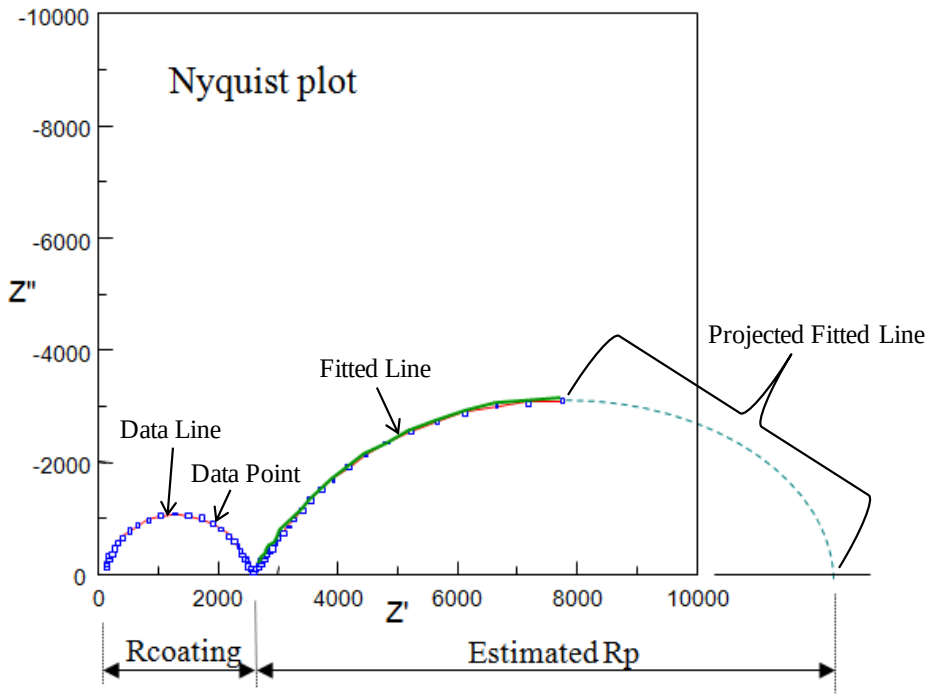

Source: FHWA.

Figure 22. Illustration. Curve fitting of EIS data.

Changes in the test conditions, particularly temperature and moisture content, can influence the LPR results significantly. However, corrosion rate measurements are useful to quantify local corrosion conditions at the time of measurement. In general, for the black bars, a corrosion rate of less than 0.1 µA/cm^2 is indicative of a passive condition (very low rate of corrosion), and the rate between 0.1 to 0.5 µA/cm^2 is considered to be low to moderate corrosion. Moderate to high corrosion and very high corrosion can be expected when the instantaneous rates of corrosion range from 0.5 to 1.0 µA/cm^2 and greater than 1.0 µA/cm^2, respectively. (Note: 1 µA/cm^2 = 6.45 µA/inch^2.)

AUTOPSY OF DOWEL BARS

At the end of the 452-d accelerated corrosion testing, all dowel bars were extracted from the concrete slabs to examine their corrosion morphologies. The following autopsy procedure was adopted:

1. Conduct visual inspection of the slab top surfaces and make damage and crack mapping.
2. Put identification tags on the bars.
3. Make two 1.5-inch-deep saw cuts across the slab width along the right-hand side and left-hand side of each bar (see figure 23).
4. Separate concrete slab segments containing dowel bars using a chisel.
5. Take photographs of the exposed bars and bar/concrete interface (see figure 24).
6. Extract the bars and preserve the concrete pieces that were in contact with the dowel bars.
7. Take concrete powder samples from bar traces for chloride analysis (see figure 25).
8. Store the bar samples in a dry area.

Source: FHWA.

Figure 23. Photo. Saw cutting of a test slab.

Source: FHWA.

Figure 24. Photo. Freshly exposed dowel bar.

CHLORIDE ANALYSIS

Due to limited budget for chloride analysis, only two concrete powder samples were extracted from a concrete fragment. As shown in figure 25, four shallow holes were drilled using a 0.1875-inch masonry drill bit into the bar/concrete interface beneath the artificial pavement joint. Because of shallow concrete cover beneath the joint, the concrete powder sample collected in this area was assumed to have the highest level of chloride accumulation. Another powder sample was collected away from the joint using the same sampling method. This powder sample represented a typical bar/concrete interface without excessive chloride contamination. The two concrete powder samples were analyzed for acid-soluble chloride according to ASTM C1152.[(25)]

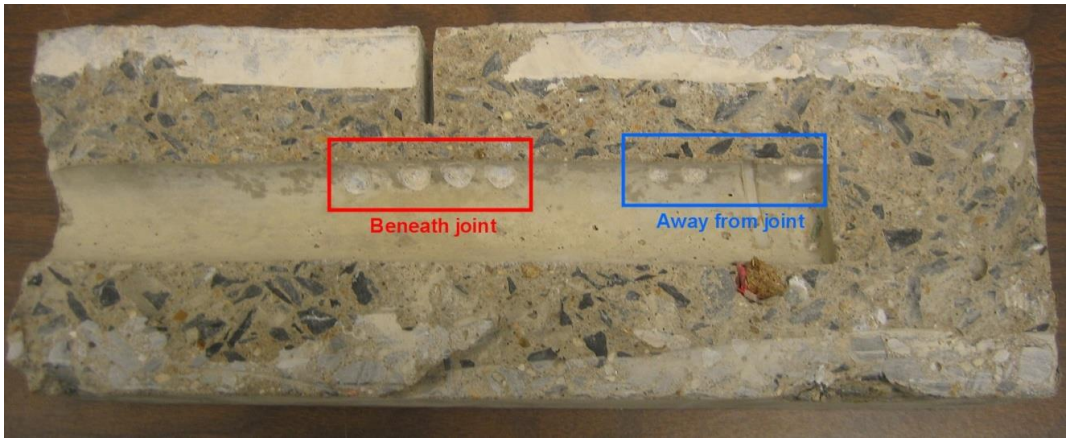

Source: FHWA.

Figure 25. Photo. Concrete sampling locations from an autopsied slab section.

CHAPTER 4. TEST RESULTS AND DISCUSSION

CORROSION POTENTIAL AND MACRO-CELL CORROSION CURRENT DENSITY

This section presents a pair of electrochemical data plots for each slab: corrosion potential versus time and $i_{macro\text{-}cell}$ versus time. These datasets are closely related to each other, and their changes with time provided useful information to determine when corrosion was initiated and how much corrosion activity occurred in the slab. In each corrosion potential plot, two black dashed lines were overlapped at –200 and –350 mV to indicate corrosion potential criteria specified in ASTM C876 in relation to the collected corrosion potential data: (1) more positive potential than –200 mV indicates a 90-percent probability of no corrosion; (2) more negative potential than –350 mV indicates a 90-percent probability of corrosion; and (3) potentials between –200 and –350 mV indicates an uncertain corrosion state.[21]

Black Bar Slab

Figure 26 and figure 27 show a corrosion potential versus time plot and an $i_{macro\text{-}cell}$ versus time plot for the black bar slab, respectively. Judging from a sudden negative potential shift, a black bar (R3) initiated corrosion first after 60 d, and another black bar (R2) became active last after 210 d. The remaining black bars initiated corrosion between 120 and 160 d of testing. Once corrosion initiated, the black bars exhibited gradual potential changes from –400 to near –600 mV_{CSE}. As expected, type 316L solid SS bar maintained the passive state at –200 mV_{CSE} throughout the testing.

As the black bars initiated corrosion one by one, the corresponding $i_{macro\text{-}cell}$ increased gradually toward a relatively low level of 0.1 $\mu A/cm^2$ until the testing was over (note that 1 $\mu A/cm^2$ = 6.45 $\mu A/inch^2$). If only the actively corroding area beneath the joint is taken into consideration, $i_{macro\text{-}cell}$ could be at least 10 times higher than what was calculated based on the entire bar surface area.

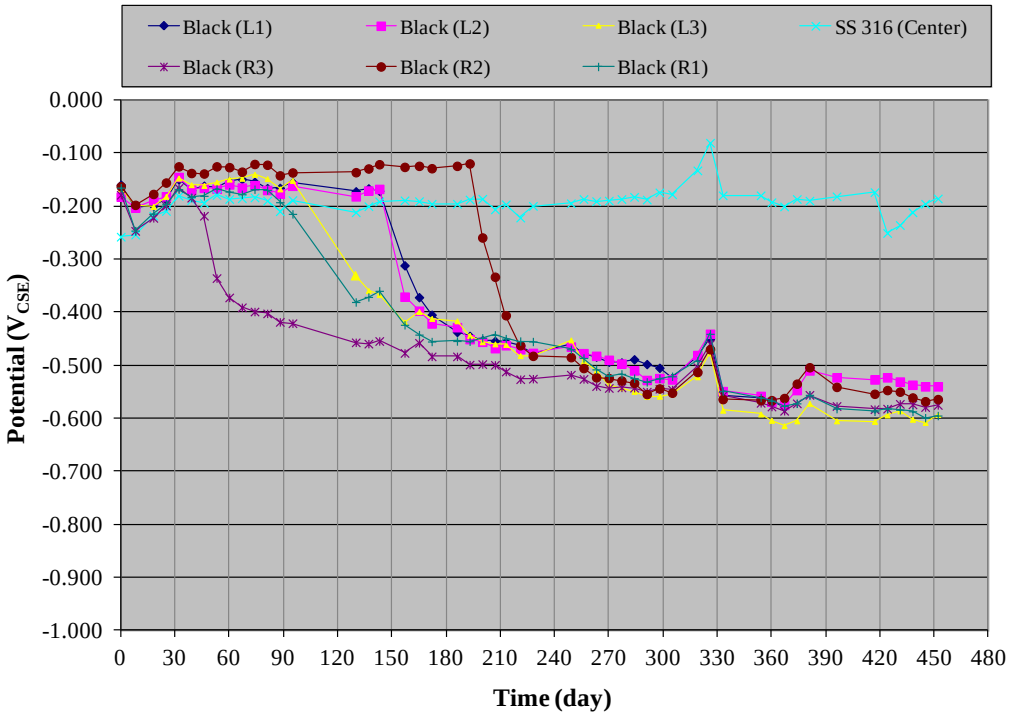

Source: FHWA.

Figure 26. Graph. Corrosion potentials versus time plot for black bar slab.

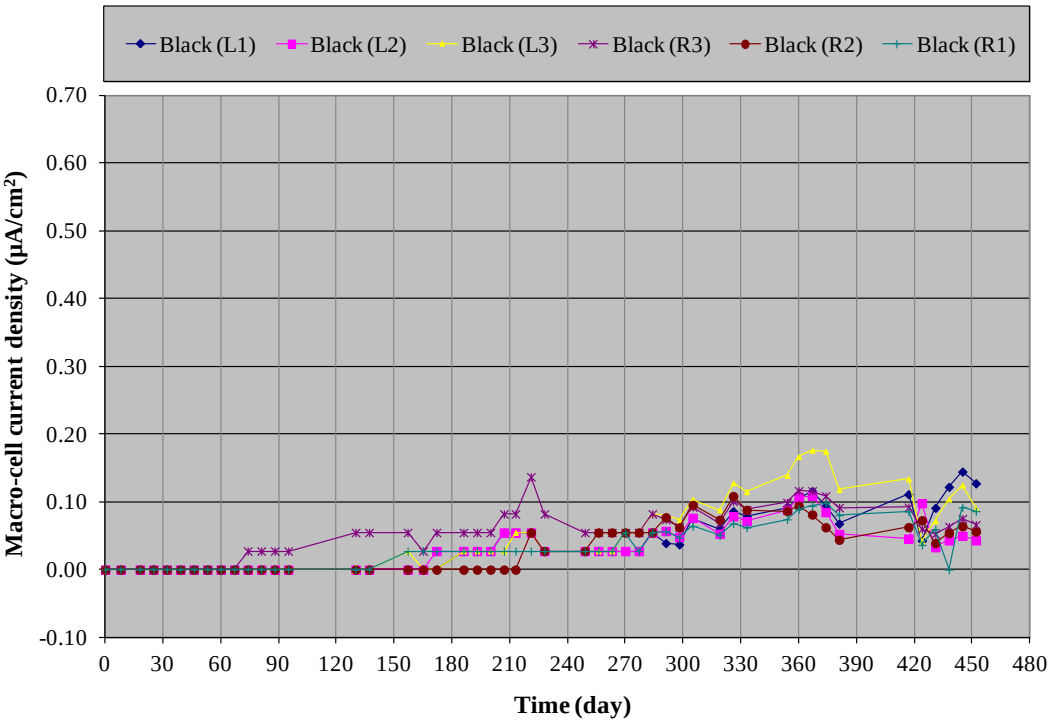

Source: FHWA.

Figure 27. Graph. $i_{macro\text{-}cell}$ versus time plot for black bar slab.

EC Bar Slab

Figure 28 and figure 29 show a corrosion potential versus time plot and an $i_{macro\text{-}cell}$ versus time plot for the EC bar slab, respectively. The EC bars containing artificial defects exhibited active corrosion potentials after 50 to 130 d, which are comparable to those of most of the black bars as presented above. A closer review of the data showed that the EC bars containing the large defects (L2 and R3, 0.59 percent) started corrosion 30 to 80 d earlier than those containing the small defects (L3 and R2, 0.07 percent). On the contrary, those with no artificial coating defects initiated corrosion at much later times: one (L1) at 330 d and the other (R1) at 380 d. These data suggest that, if coating quality is good with minimal coating damage, time-to-corrosion initiation can be at least four times longer compared with those containing the large defects. Once corrosion initiated, the EC bars stayed at a range between –400 and –600 mV_{CSE} like the black bars. Again, type 316L solid SS bar remained in a passive state at –200 mV_{CSE} throughout the testing.

The corroding EC bars exhibited a very low-level $i_{macro\text{-}cell}$, which appears to be less than 50 percent of the black bars shown in figure 27. However, if only bare areas exposed in the coating defects are considered, the EC bars could produce nearly 100 times higher $i_{macro\text{-}cell}$ than the black bars. More will be discussed in the autopsy section.

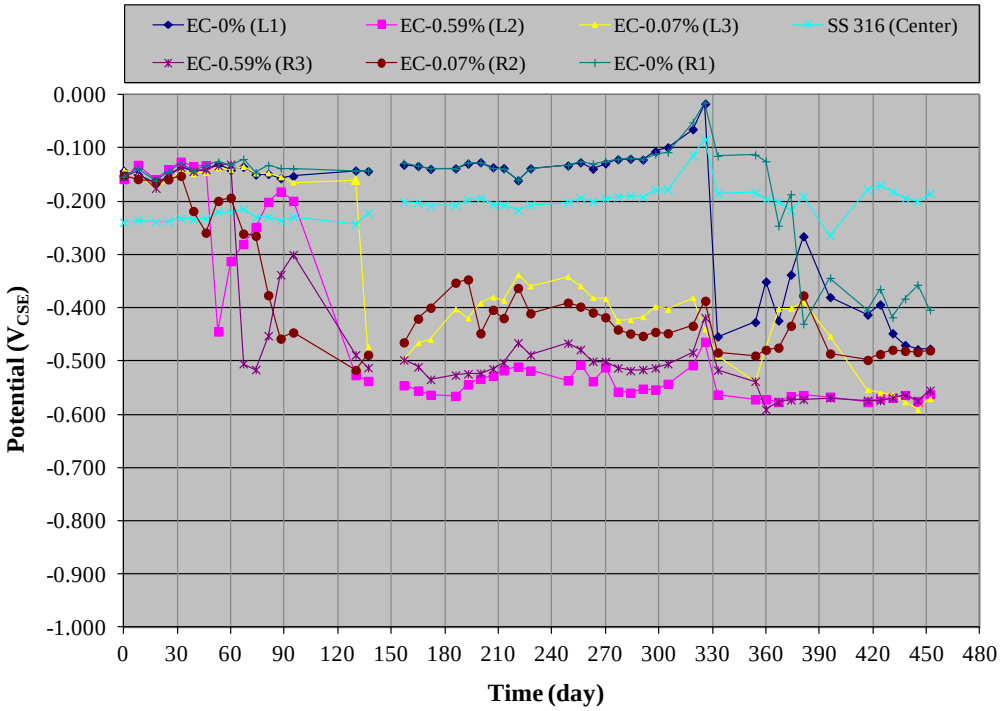

Source: FHWA.

Figure 28. Graph. Corrosion potentials versus time plot for EC bar slab.

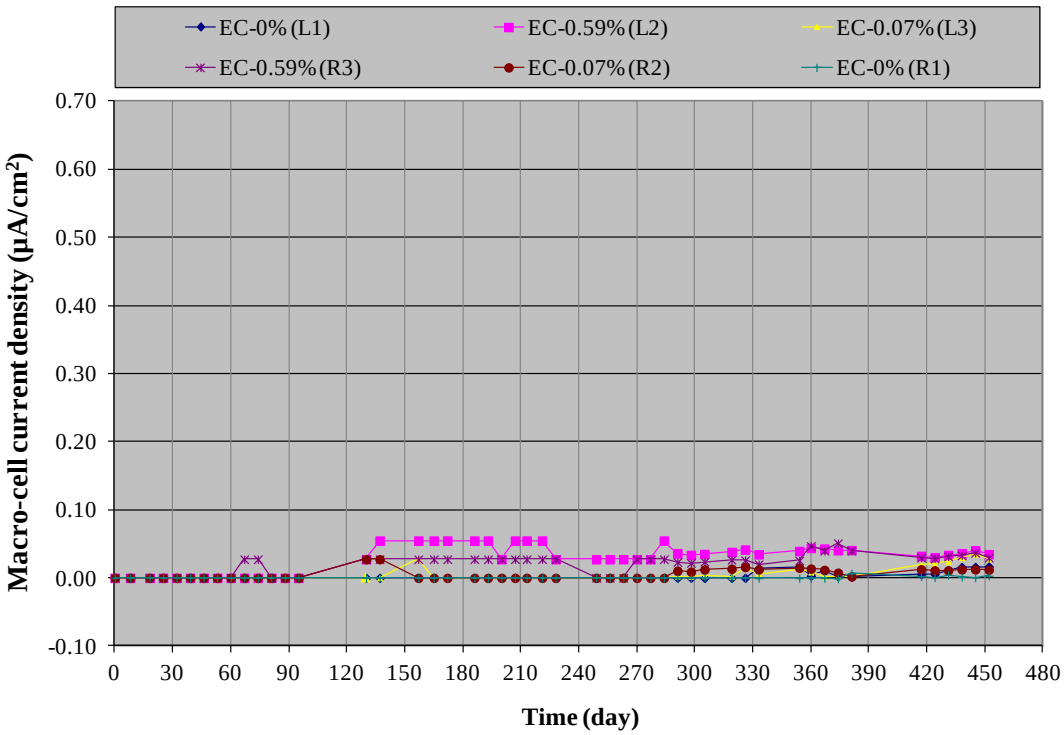

Source: FHWA.

Figure 29. Graph. $i_{macro\text{-}cell}$ versus time plot for EC bar slab.

HDG Bar Slab

Figure 30 and figure 31 show a corrosion potential versus time plot and an $i_{macro\text{-}cell}$ versus time plot for the HDG bar slab, respectively. Since the HDG bars were coated with an active zinc layer that inherently shows very negative corrosion potential, the measured corrosion potentials varied between –450 and –700 mV_{CSE} regardless of artificial defect size. It is thought that passivation of the zinc was responsible for the initial potential movement in the positive direction observed between 8 and 90 d. The corrosion potentials became more negative between 180 and 240 d before becoming more positive again. Contrary to this, the type 316L solid SS bar remained at near –200 mV_{CSE} throughout the testing.

As expected, the HDG bars produced much higher $i_{macro\text{-}cell}$ than the black bars and EC bars due to the sacrificial role of the zinc coating. However, no effect of defect size can be recognized in the data. This means that the HDG bars were corroding uniformly, rather than localized galvanic corrosion of the zinc coating around the defects. The first current surge observed between 0 and 30 d was due to an actively corroding zinc layer when it encountered fresh concrete mix. The second current surge was observed corresponding to the second potential dip occurring between 180 and 240 d.

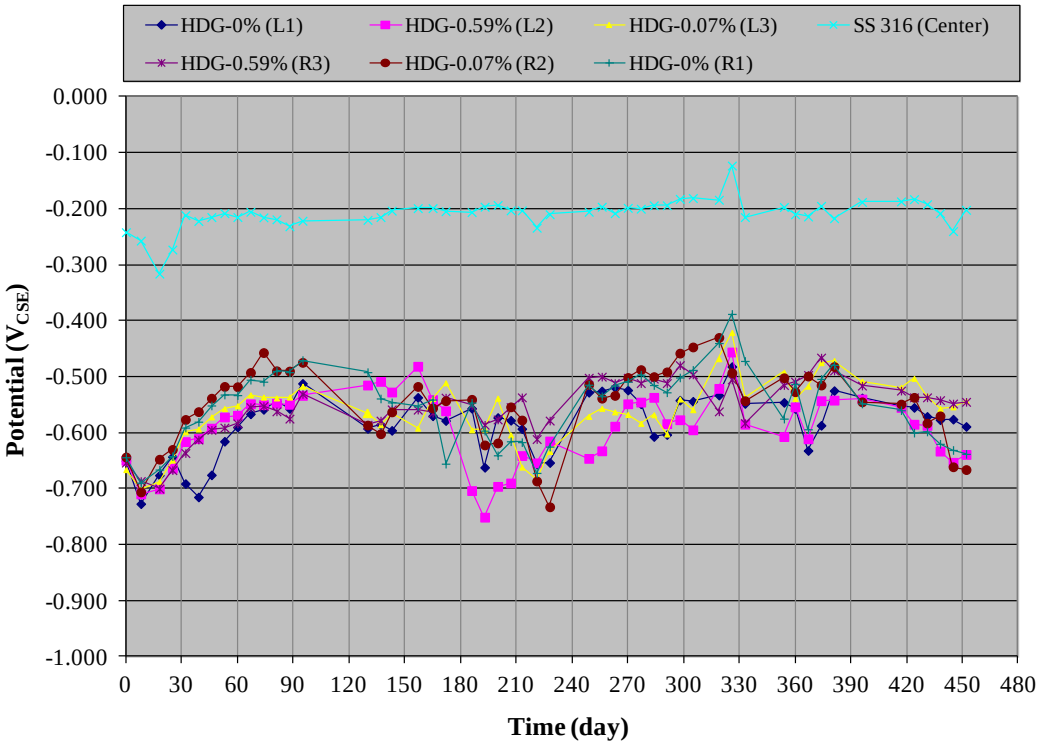

Source: FHWA.

Figure 30. Graph. Corrosion potentials versus time plot for HDG bar slab.

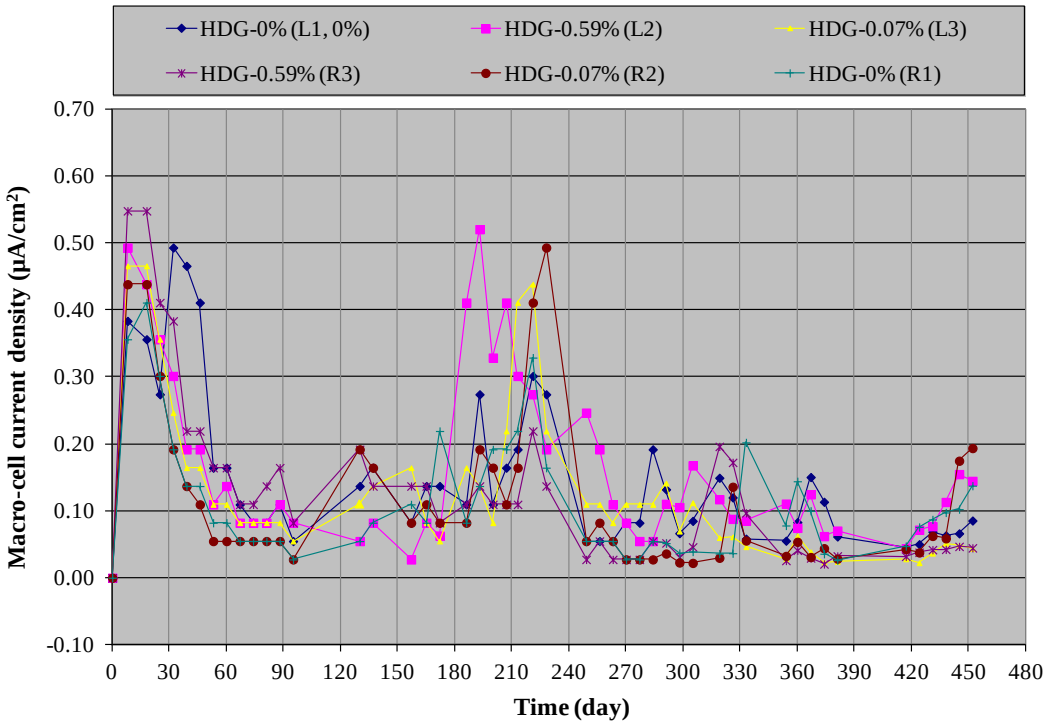

Source: FHWA.

Figure 31. Graph. $i_{macro\text{-}cell}$ versus time plot for HDG bar slab.

ZC Bar Slab

Figure 32 and figure 33 show a corrosion potential versus time plot and an $i_{macro\text{-}cell}$ versus time plot for the ZC bar slab, respectively. Even though this material also has a zinc layer like the HDG, the ZC bars started with more positive corrosion potentials than the HDG bars (–400 versus –650 mV_{CSE}). After that, the ZC bars exhibited steadily more negative potentials with time. At the end, the ZC bars showed about –100 mV more negative corrosion potential than the HDG. Similar to the HDG bar case, the artificial defects did not yield any noticeable changes.

The $i_{macro\text{-}cell}$ data show a steadily increasing trend with time in association with the gradually decreased corrosion potential, but there was a large variation of $i_{macro\text{-}cell}$ data accompanied by four distinctive current surges. The maximum $i_{macro\text{-}cell}$ observed at the peak of the surges was about 15 percent higher than that observed at the single peak of the HDG $i_{macro\text{-}cell}$ data. The $i_{macro\text{-}cell}$ data indicate that the ZC produced the largest corrosion current among the entire bar materials tested in this study.

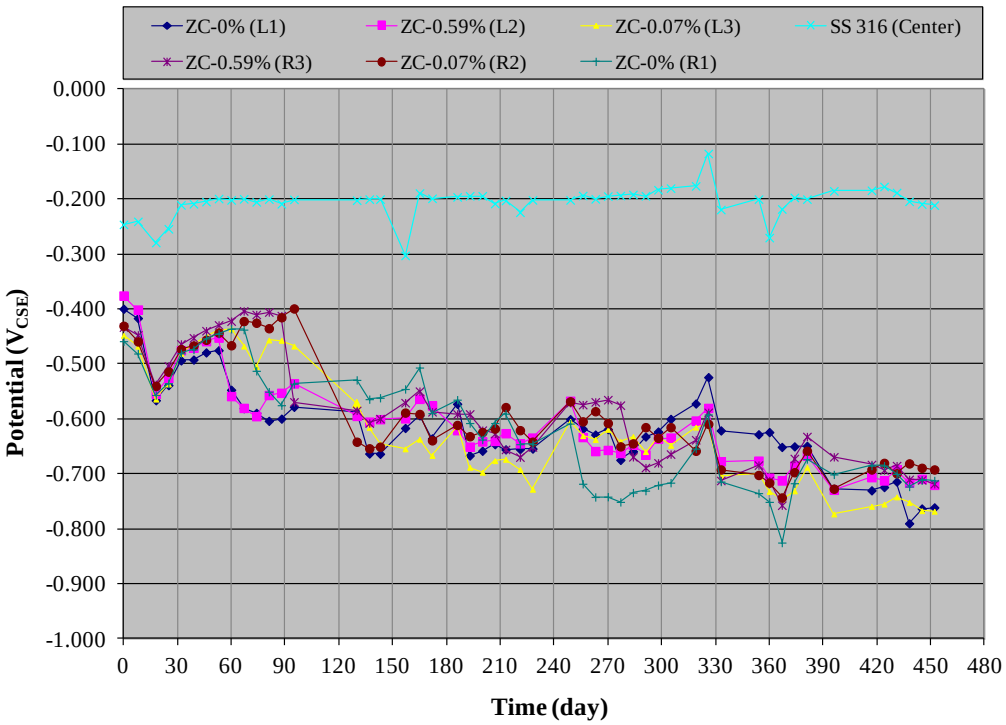

Source: FHWA.

Figure 32. Graph. Corrosion potentials versus time plot for ZC bar slab.

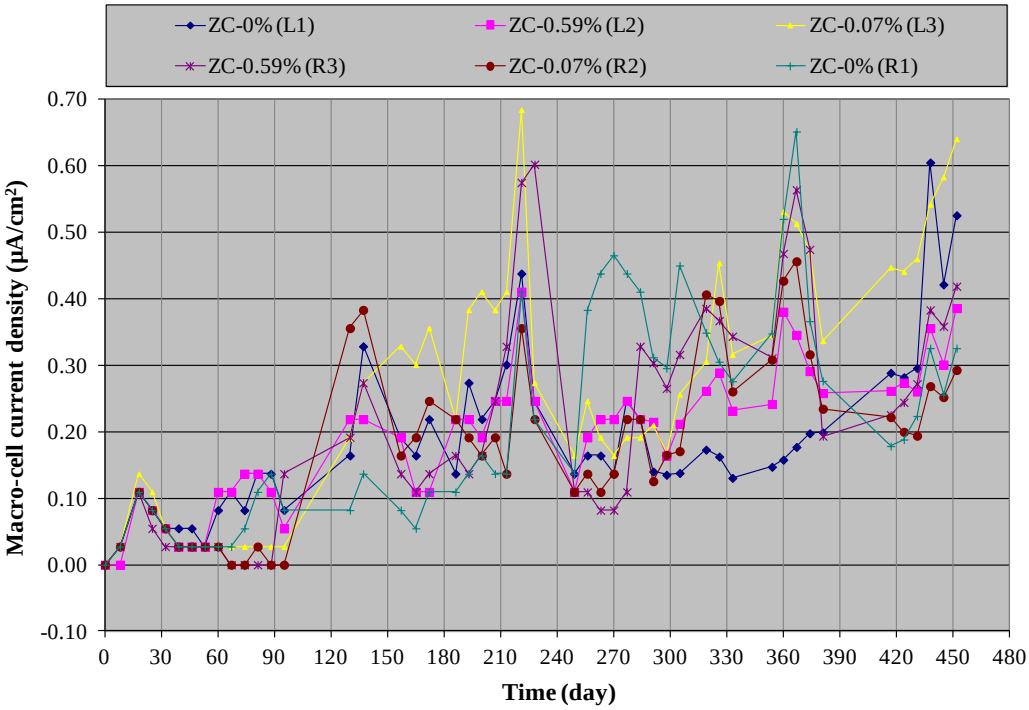

Source: FHWA.

Figure 33. Graph. $i_{macro\text{-}cell}$ versus time plot for ZC bar slab.

SCA/SCB Bar Slab

Figure 34 and figure 35 show a corrosion potential versus time plot and an $i_{macro\text{-}cell}$ versus time plot for the SCA/SCB bar slab, respectively. The SCA and SCB bars behaved similarly to type 316L solid SS bars except for two bars containing the large defect. An SCA bar with the 0.59-percent defect (L2) initiated corrosion only after 50 d and became passive again after 150 d. On the other hand, an SCB bar with the same defect size (R2) started corrosion after 135 d and remained active until the end.

The $i_{macro\text{-}cell}$ data indicate virtually zero activity, regardless of cladding type and defect size. The negligible $i_{macro\text{-}cell}$ must be due to small potential differences that are the driving force between each of the SCA/SCB bars (macro-anode) and type 316L solid SS bar (macro-cathode).

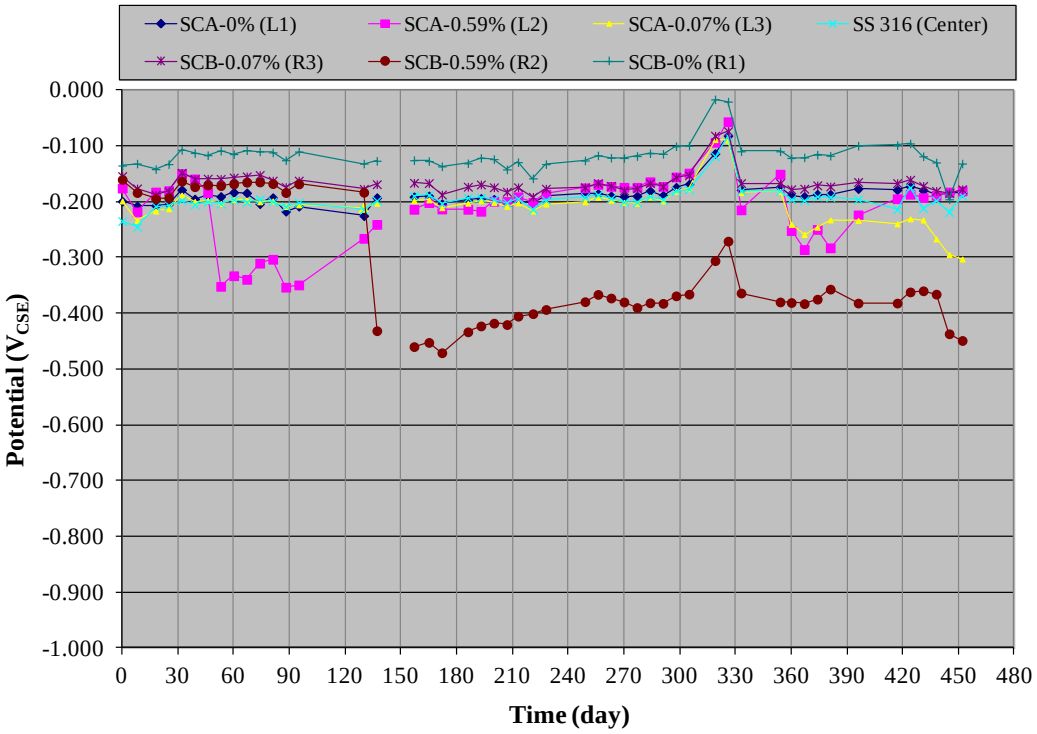

Source: FHWA.

Figure 34. Graph. Corrosion potentials versus time plot for SCA/SCB bar slab.

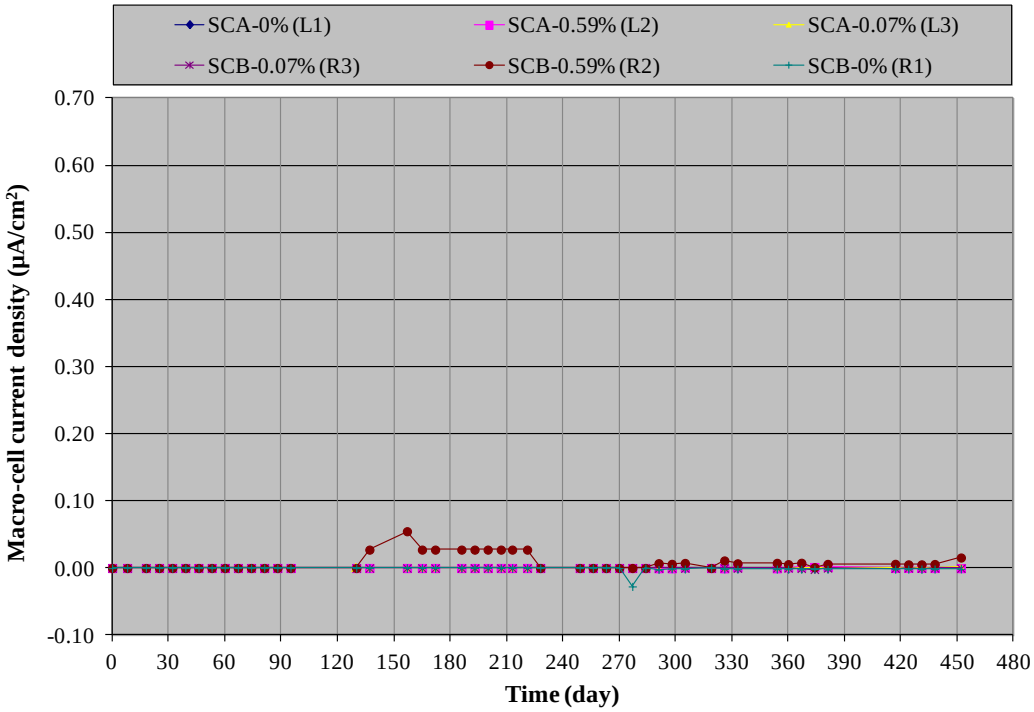

Source: FHWA.

Figure 35. Graph. $i_{macro\text{-}cell}$ versus time plot for SCA/SCB bar slab.

SCC Bar Slab

Figure 36 and figure 37 show a corrosion potential versus time plot and an $i_{macro\text{-}cell}$ versus time plot for the SCC bar slab, respectively. The black bar placed in the center of the slab as the macro-anode started corrosion around 165 d after testing. Its corrosion initiation time is within the range observed in the black bar potential plot (see figure 24). An SCC bar (L3) with the 0.07-percent defect initiated corrosion slightly earlier (150 d) than the black bar and remained active for most of the testing duration. Two more SCC bars (R3 and L2) with the 0.59-percent defect started corrosion at 250 and 315 d, respectively. Both defect-free SCC bars (L1 and R1) and the other 0.07-percent defect bar (R2) behaved like type 316L SS bar throughout the testing. There is no clear trend related to defect size on corrosion initiation time.

Because the black bar was the macro-anode and each of the SCC bars was the macro-cathode, the $i_{macro\text{-}cell}$ data presented in figure 37 is macro-cell corrosion current density of the black bar when it was coupled to individual SCC bars. The $i_{macro\text{-}cell}$ data exhibited increasingly higher $i_{macro\text{-}cell}$ with time. This means that the black bar was corroding more due to increasingly accumulated chloride ions over time. The highest $i_{macro\text{-}cell}$ was about 0.4 $\mu A/cm^2$, which is nearly four times higher than the black bar slab case presented in figure 27. One possible reason for much higher $i_{macro\text{-}cell}$ may be due to the black bar's prolonged time being the single macro-anode. Although each of the black bars in the black bar slab also served as the macro-anode, they were connected to the solid SS bar only for a relatively short duration whenever the macro-cell corrosion current was measured.

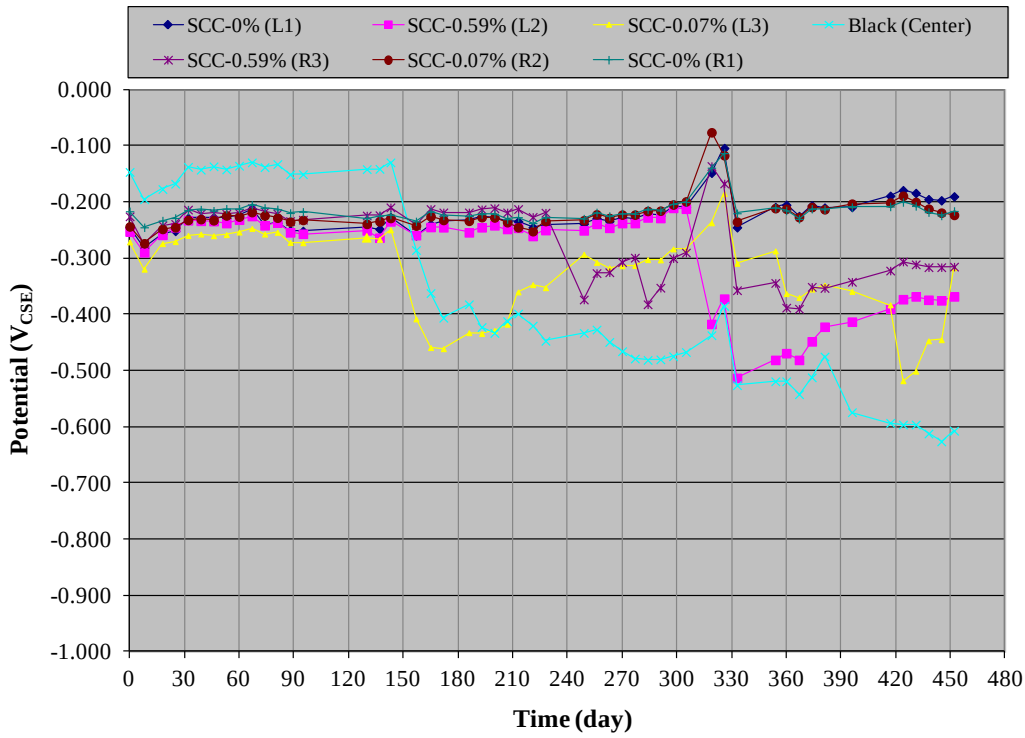

Source: FHWA.

Figure 36. Graph. Corrosion potentials versus time plot for SCC bar slab.

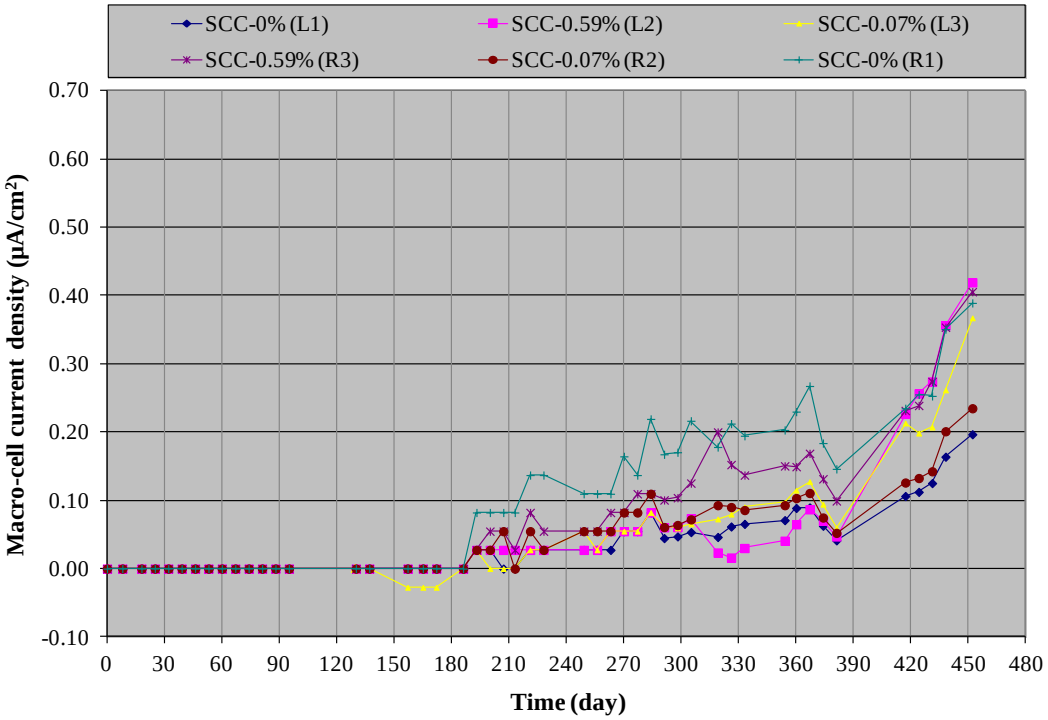

Source: FHWA.

Figure 37. Graph. $i_{macro\text{-}cell}$ versus time plot for SCC bar slab.

Assorted Bar Slab

Figure 38 and figure 39 show a corrosion potential versus time plot and an $i_{macro\text{-}cell}$ versus time plot for the assorted bar slab, respectively. As table 4 indicated, none of the bars tested in this slab contained artificial defects, and a bond breaker was not applied. Also, type 316L SS bar was not included as the macro-cathode. Instead, an SCC bar served as the macro-cathode, and each of the other bars was temporarily connected as the macro-anode to the SCC bar when macro-cell corrosion current was measured.

Four bar materials (black, EC, SCB, and SCC) included in the assorted slab exhibited the same corrosion potential trend as the same materials included in their own slabs. The defect-free SCA started corrosion after 390 d, whereas the other defect-free SCA bar in the SCA/SCB slab did not show any sign of corrosion (see figure 34). The HDG and ZC bars also showed more active corrosion behaviors than those in the HDG and ZC slabs. For example, the ZC bar exhibited a gradually positive corrosion potential trend until a sudden potential drop was observed after 370 d and remained near –900 mV_{CSE}. This potential behavior was not observed in the ZC slab (see figure 32). The HDG bar maintained a similar corrosion potential trend until 210 d, but it also experienced a potential shift at 230 d in the negative direction followed by a gradual movement in the positive direction with time. This potential behavior was not observed in the HDG slab (see figure 30). It is speculated that the different corrosion potential behaviors of the bar materials with a zinc surface might be related to the absence of the bond breaker, which could alter the chemistry at the zinc/concrete interface. In other words, the bond breaker might contribute to suppressing the corrosion of zinc coatings.

The $i_{macro\text{-}cell}$ data of the HDG and ZC bars indicated much higher corrosion rates than those observed from the HDG and ZC slabs. This finding corresponds to their active corrosion behavior based on very active corrosion potential tendency as discussed above. The other bar materials exhibited negligible $i_{macro\text{-}cell}$, which is consistent with $i_{macro\text{-}cell}$ data observed from their own slabs.

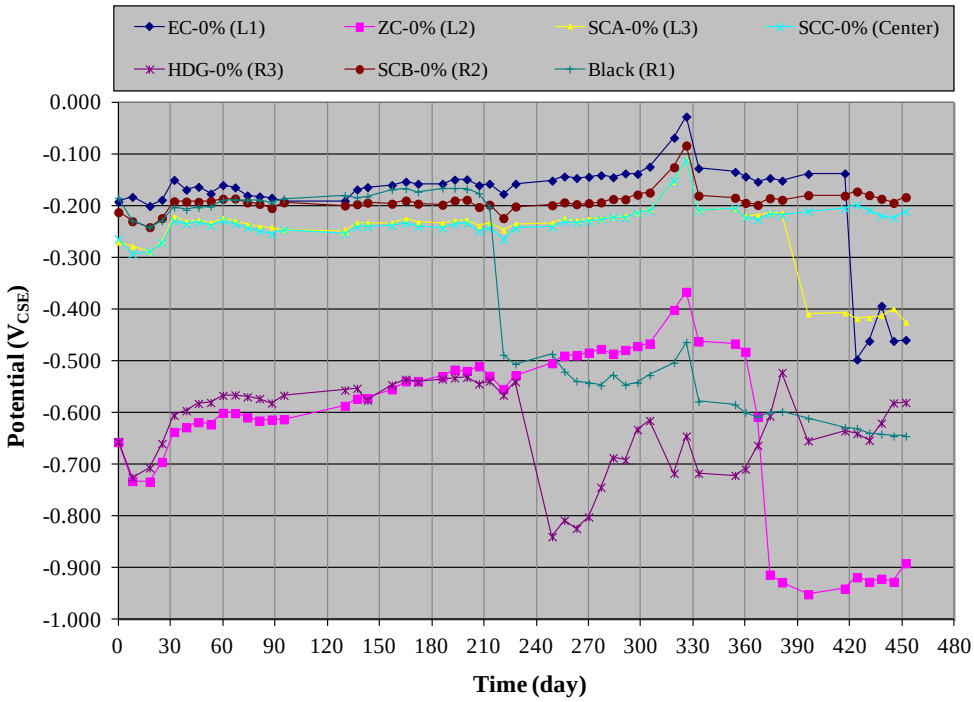

Source: FHWA.

Figure 38. Graph. Corrosion potentials versus time plot for assorted bar slab.

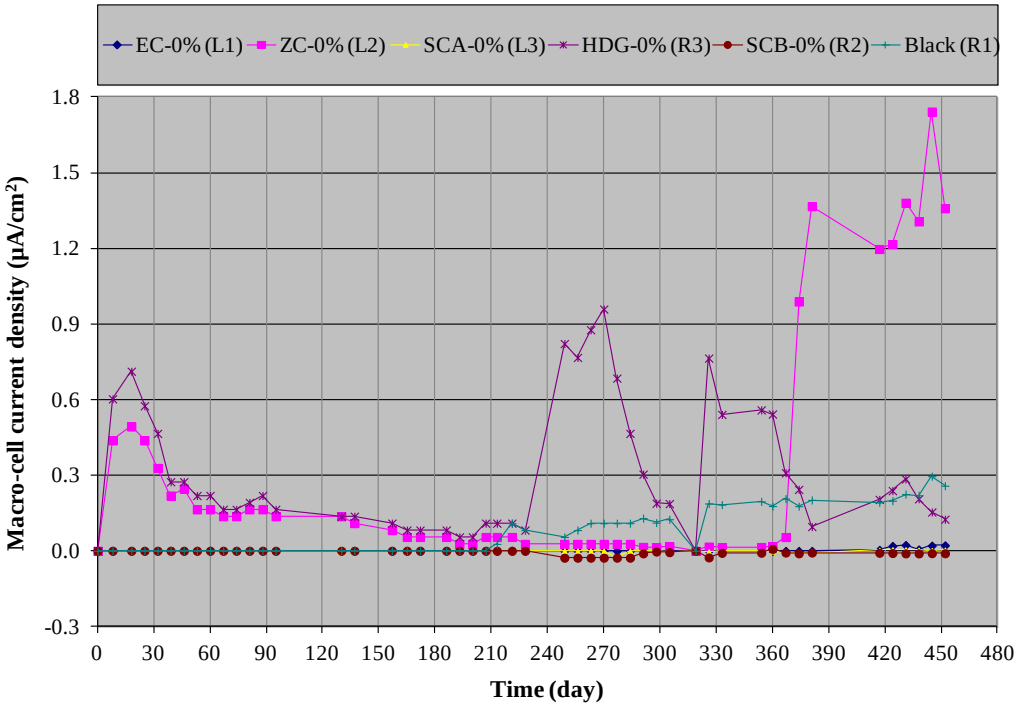

Source: FHWA.

Figure 39. Graph. $i_{macro\text{-}cell}$ versus time plot for assorted bar slab.

MEAN MACRO-CELL CORROSION CURRENT DENSITY

Figure 40 summarizes mean $i_{macro\text{-}cell}$ values based on individual $i_{macro\text{-}cell}$ data points grouped by bar type and defect size over the entire testing period of 452 d. The ZC bar showed the highest mean $i_{macro\text{-}cell}$, followed by the HDG and the SCC. As mentioned earlier regarding the SCC data, their mean $i_{macro\text{-}cell}$ values actually represented those of the black bar in connection with the individual SCC bars. The effect of defect size was not apparent on these SCC bars. The other bar materials (EC, SCA, and SCB) exhibited very low mean $i_{macro\text{-}cell}$ values. The EC and the SCB bars containing the large defect show slightly higher mean $i_{macro\text{-}cell}$ than those bars with small or no defects.

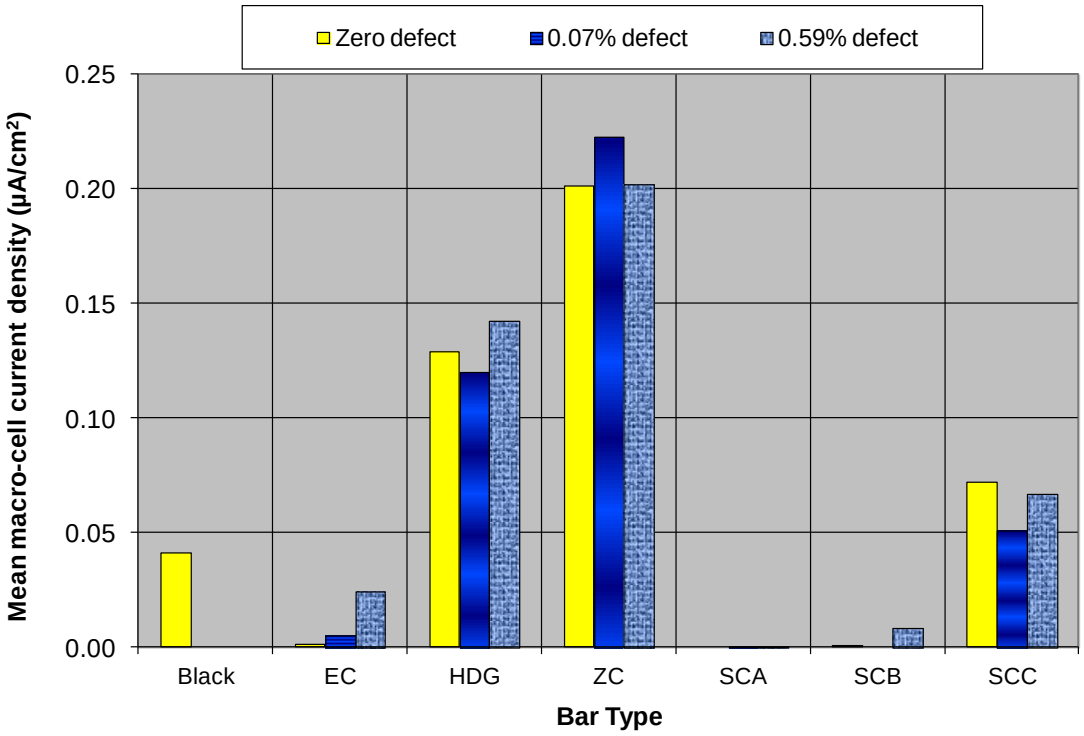

Source: FHWA.

Figure 40. Graph. Mean macro-cell corrosion current densities.

AC RESISTANCE

Figure 41 through figure 47 show the AC resistance versus time plots for individual slabs. While the majority of them showed a relatively small variation of AC resistance ranging from 100 to 600 Ω, the EC and HDG slabs exhibited much higher resistances. Two defect-free HDG bars exceeded the 600 Ω after 320 d, as shown in figure 45. All of the EC bars exhibited much higher AC resistance than the bare dowel bars thanks to the epoxy coating. Their resistance values gradually increased with time, independent of defect size. Among them, two defect-free EC bars showed a significant increase beyond 17,000 Ω in an abrupt fashion and then suddenly decreased to the similar level as the other bars at 330 d (L1) and 380 d (R1). It is not known why this type of extraordinary behavior took place. Interestingly, the timing of the sudden resistance decrease coincided with their corrosion initiation time (see figure 28). It can be deduced that the initially defect-free EC bars developed coating defects in the concrete, which could result in the reduced AC resistances. The defect-free EC bar (L1) in the assorted bar slab also exhibited gradual resistance increase with time. The highest resistance measured was 2,500 Ω, which was almost one order of magnitude lower value compared with the other defect-free EC bars. The lower maximum resistance may be due to unidentified coating holidays that were pre-existed on the coating surface. However, its resistance also dropped suddenly at 430 d. This event also corresponded to the corrosion initiation of the same bar, as shown in figure 38.

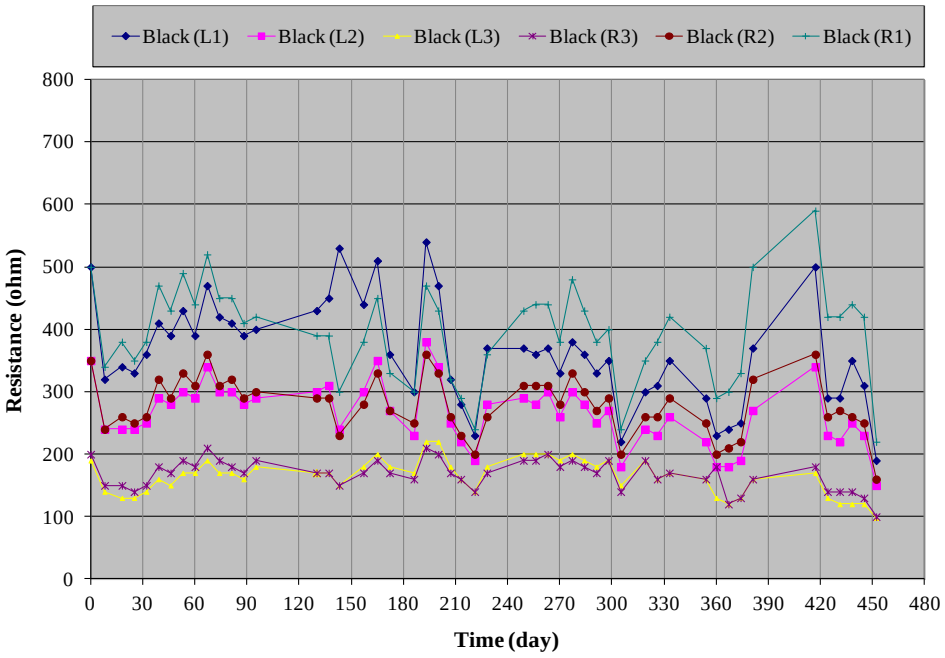

Source: FHWA.

Figure 41. Graph. AC resistance versus time plot for black bar slab.

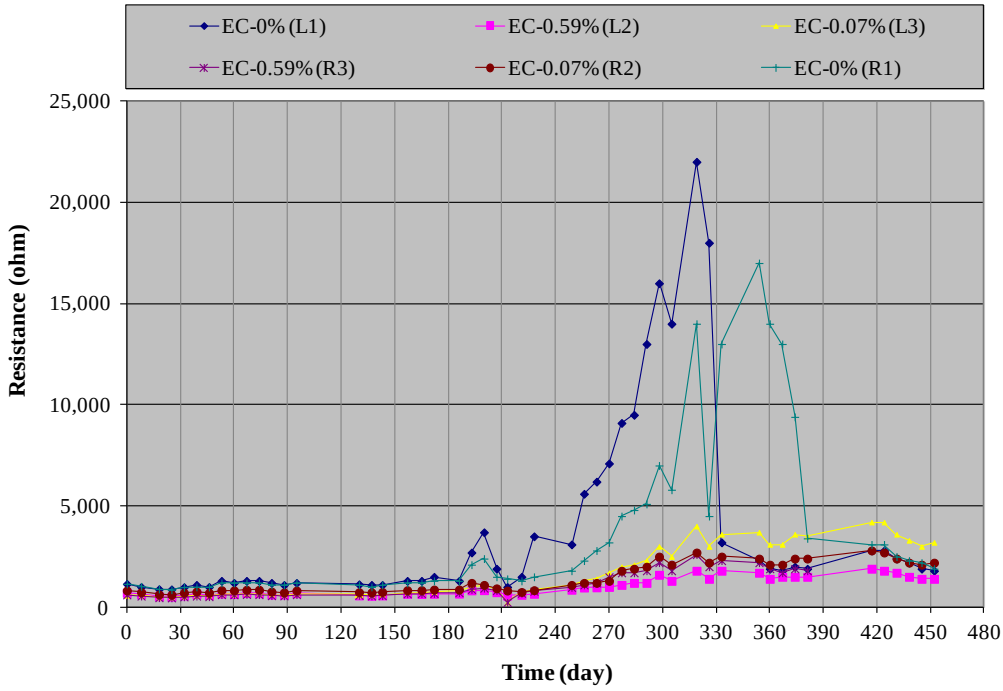

Source: FHWA.

Figure 42. Graph. AC resistance versus time plot for EC bar slab.

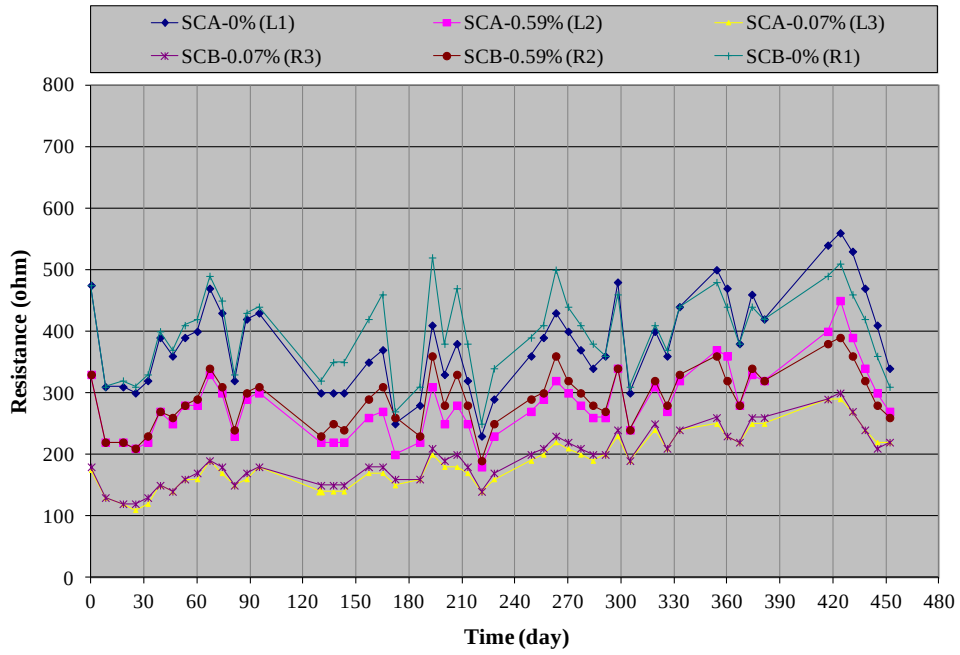

Source: FHWA.

Figure 43. Graph. AC resistance versus time plot for SCA/SCB bar slab.

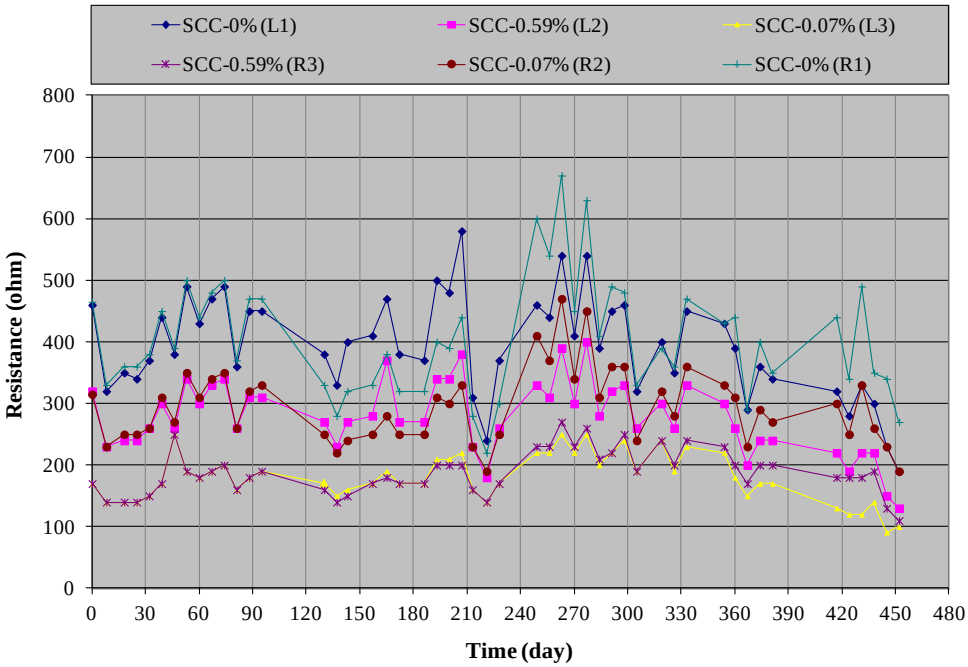

Source: FHWA.

Figure 44. Graph. AC resistance versus time plot for SCC bar slab.

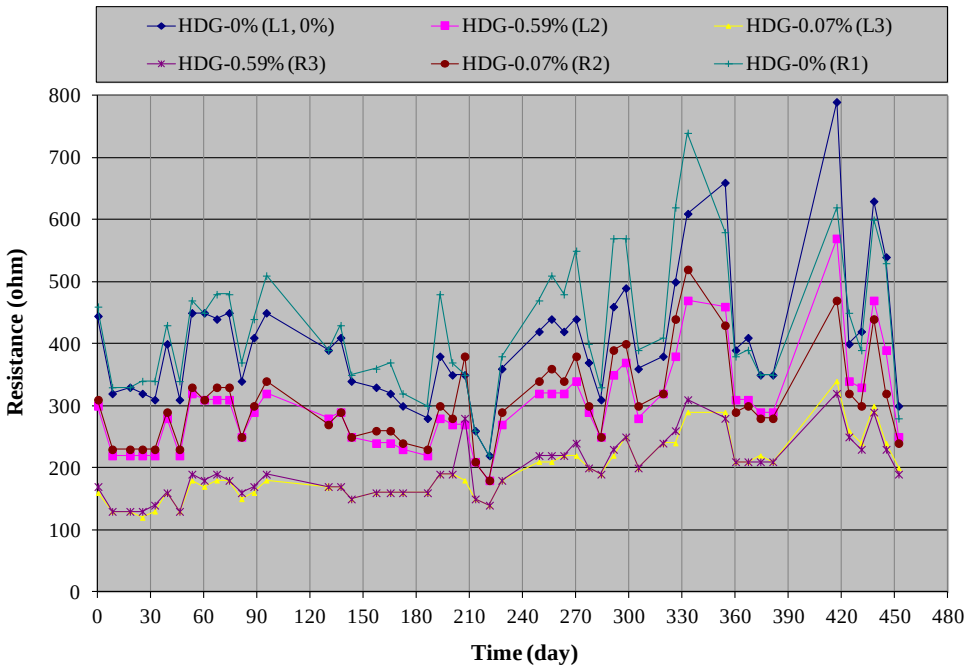

Source: FHWA.

Figure 45. Graph. AC resistance versus time plot for HDG bar slab.

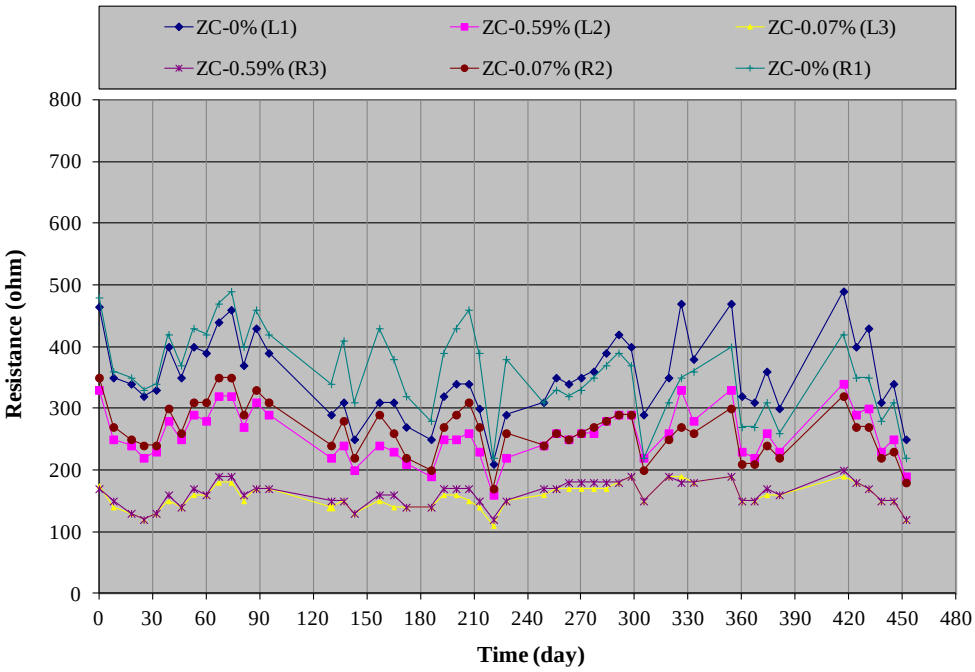

Source: FHWA.

Figure 46. Graph. AC resistance versus time plot for ZC bar slab.

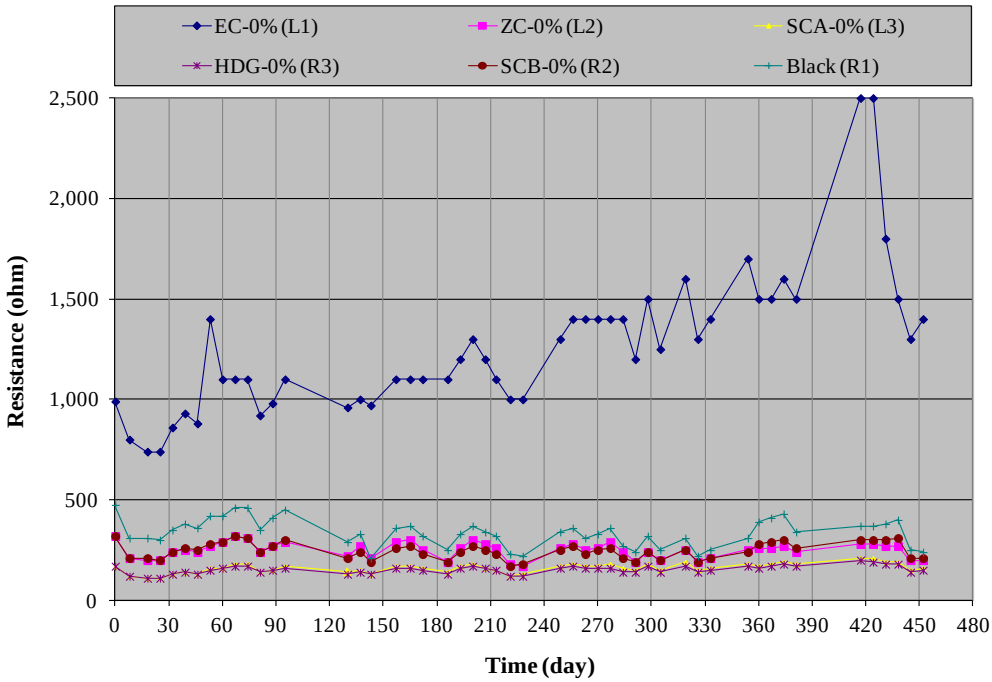

Source: FHWA.

Figure 47. Graph. AC resistance versus time plot for assorted bar slab.

MEAN CORROSION RATE

Figure 48 shows typical experimental LPR data of individual bar materials. (Figure 21 presented a schematic of the LPR data; all of the solid SS and SC bars can be related to SS.) This figure illustrates how the relative position of the potential and the relative magnitude of the current range in the LPR plots can vary depending on different bar materials: more corrosion-resistant materials show more positive corrosion potential and smaller current magnitude in association with a larger slope. For example, two more corrosion-resistant bars, labeled SS and EC, exhibit more positive corrosion potential and much smaller current range associated with steeper slopes than the less corrosion resistant bars, labeled HDG, black, and Zn-clad.

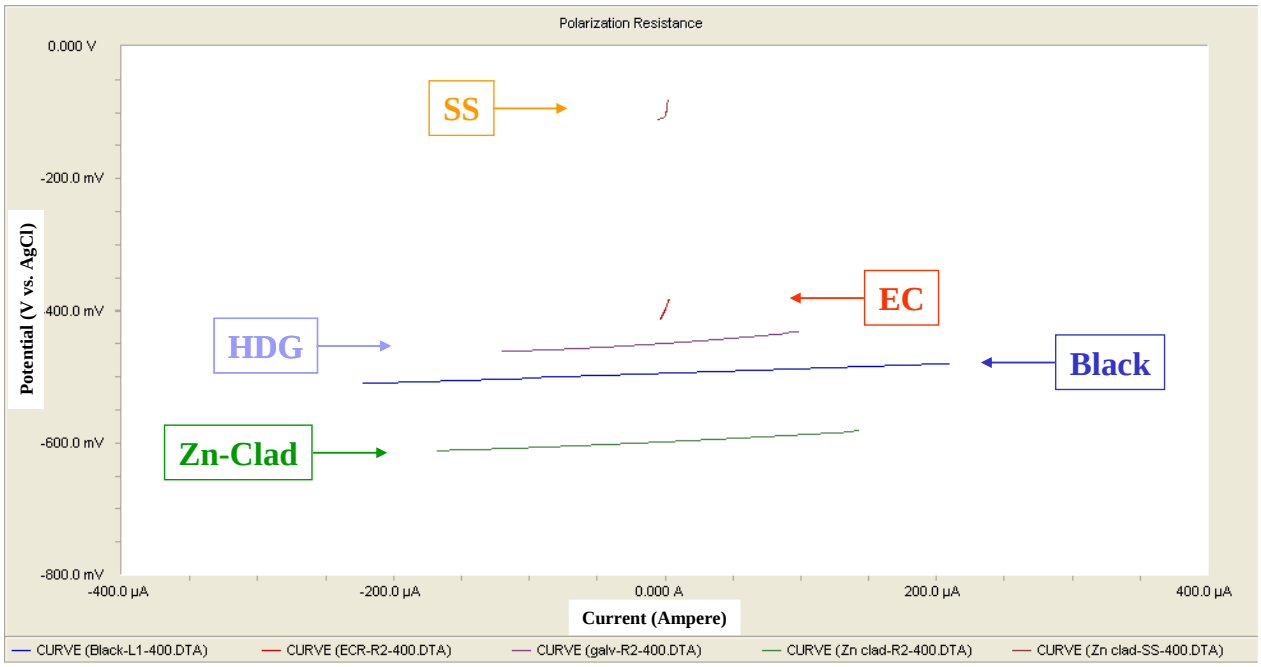

Source: FHWA.

Figure 48. Illustration. Examples of experimental LPR data.

Figure 49 summarizes the mean corrosion rate values of each bar material that are grouped by time of measurement (baseline versus final at 452 d) and defect size (0, 0.07, and 0.59 percent). When the bars were exposed to chloride-free concrete, baseline corrosion rate was very low. The highest mean corrosion rate of 0.15 mil/yr was observed with black bars, followed by 0.1 and 0.05 mil/yr for HDG and ZC bars, respectively. The others exhibited negligible corrosion rates. After excessive chloride ions were accumulated at the bar/concrete interface near the end of the testing, the same bars showed 4 to 10 times higher corrosion rates compared with their baseline data. The most significant increase was made by the ZC bars, which had shown the most active corrosion behavior in terms of corrosion potential and $i_{macro\text{-}cell}$ data (which is to be expected, since the zinc coating acts as a large, exposed anode). At the end of the accelerated corrosion testing, the ZC and black bars yielded the highest mean corrosion rate. As observed in the $i_{macro\text{-}cell}$ data, the HDG bar exhibited the second highest mean corrosion rate. The other bars did not produce recognizable corrosion rates. Even though ZC and HDG showed a trend of decreased mean corrosion rate as artificial defect size increased, especially HDG, the significance of this observation is not clear. The other bars did not show such a trend.

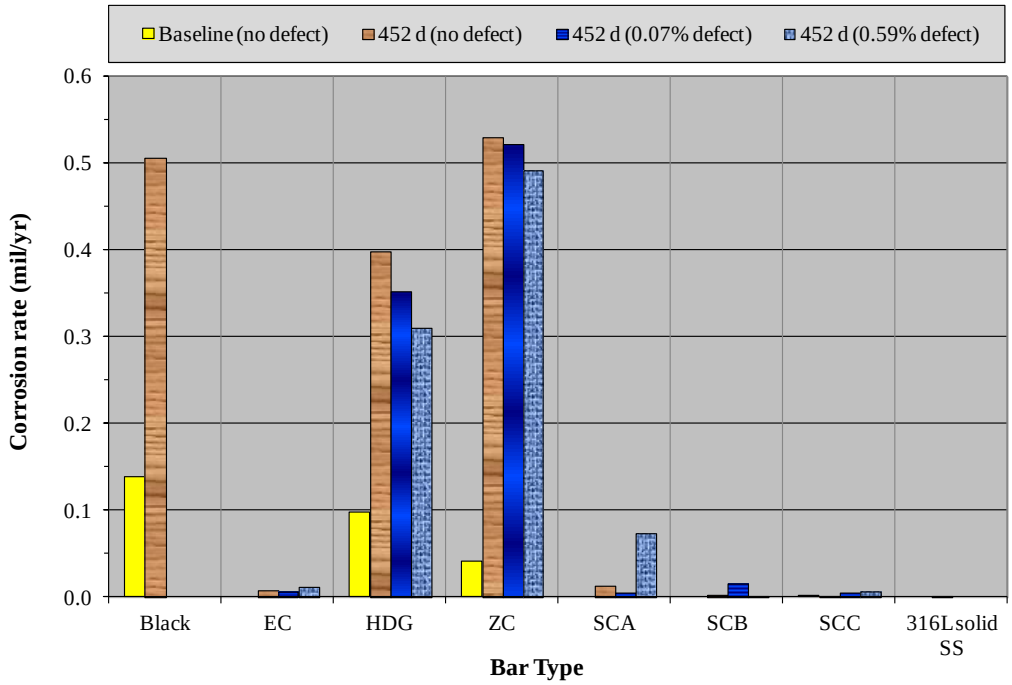

Source: FHWA.

Figure 49. Graph. Mean corrosion rates determined by LPR method.

CHLORIDE ANALYSIS

Each of the two concrete powder samples taken according to figure 25 was analyzed to determine representative chloride concentration at the joint and away interface, respectively. Mean acid-soluble chloride concentrations were 11,072 ppm (35 lb/yd^3) by weight of sample beneath the joint and 1,130 ppm (4 lb/yd^3) away from the joint, near the end of the bar. Rapid ingress of chloride ions through the 0.5-inch shallow concrete cover at the bottom of the simulated joint resulted in such a high chloride concentration. On the other hand, normal chloride diffusion process through the 2.0-inch concrete cover yielded a low-level chloride contamination during the 452 d of the accelerated corrosion testing. The former is considered an exceptionally high level of chloride contamination that certainly makes most metallic bars corrode as intended. The latter exceeded the chloride threshold for the black bars, but it was not sufficient to induce the corrosion of some other corrosion resistant bars.

AUTOPSY AND CORROSION MORPHOLOGY

Figure 50 shows a group photograph of all extracted bars. They exhibited various physical conditions that reflected the degree of corrosion and correlated reasonably well with the non-destructively collected electrochemical data. In the photographs illustrating the concrete slabs when visible cracks originating from the simulated pavement joint were observed on the slab's top surface, they were traced with a red permanent marker for better photographic documentation. Before taking a group photograph of as-extracted bars that came out of each slab, they were arranged according to their relative location in the slab so that their physical condition

can be easily compared with that of the top surface. The short black lines at the front ends of the extracted bars indicated 12 o'clock orientation (facing the top surface and simulated joint) when they were in the test slabs. The following section discusses autopsy results based on the observed corrosion morphologies.

Source: FHWA.

Figure 50. Photo. Overview of the entire extracted dowel bars.

Black Bar Slab

Figure 51 shows the top surface of the black bar slab that contained five visible cracks. The cracks were formed directly above five out of six black bars. Figure 52 shows physical condition of the as-extracted black bars in the same position and orientation as they were in the slab. As expected, all of the black bars exhibited more or less severe corrosion while a type 316L solid SS bar was clean without signs of corrosion.

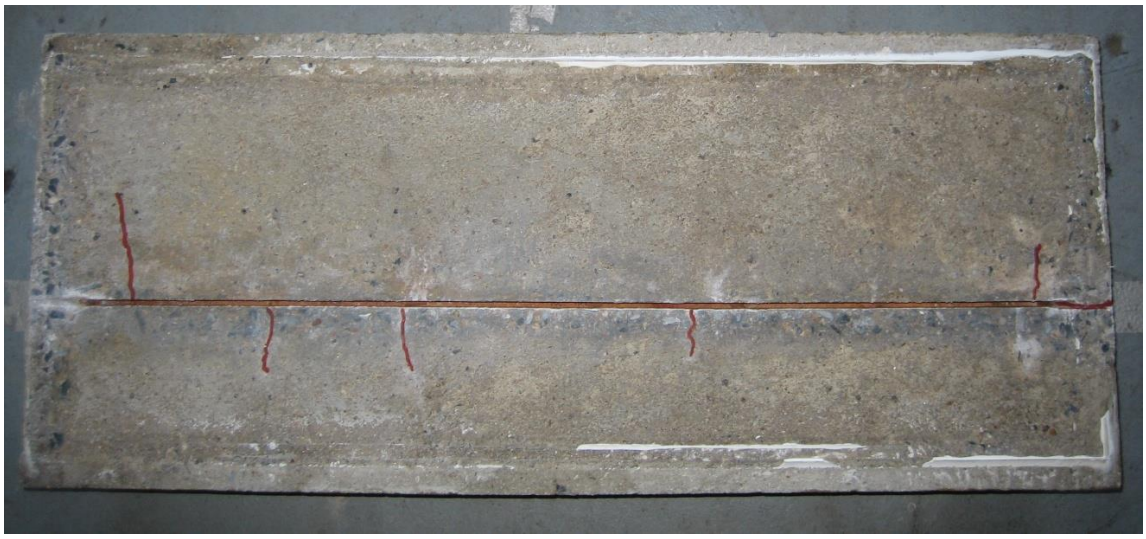

Source: FHWA.

Figure 51. Photo. Top surface condition of black bar slab before autopsy.

Source: FHWA.

Figure 52. Photo. Condition of as-extracted bars from black bar slab.

Figure 53 shows a representative condition of the black bars when they were exposed during the slab demolition process. Figure 54 and figure 55 show appearance of top and bottom sides of an as-extracted bar. The top side suffered from heavy corrosion damage as it faced the joint, but the bottom side was still in good condition. Figure 56 shows another freshly exposed black bar that exhibited greenish and black corrosion products, suggesting very intensive corrosion through a chloride-inducing acidification process in a less oxygen-available environment. Figure 57 shows a cleaned black bar segment that revealed the deepest pit (48 mil) surrounded by numerous shallow pits. The intensity of the corrosive environment created during the accelerated corrosion testing can be inferred by this corrosion morphology.

Source: FHWA.

Figure 53. Photo. Condition of an exposed black bar (BL3).

Source: FHWA.

Figure 54. Photo. Top side of the bar shown in figure 53.

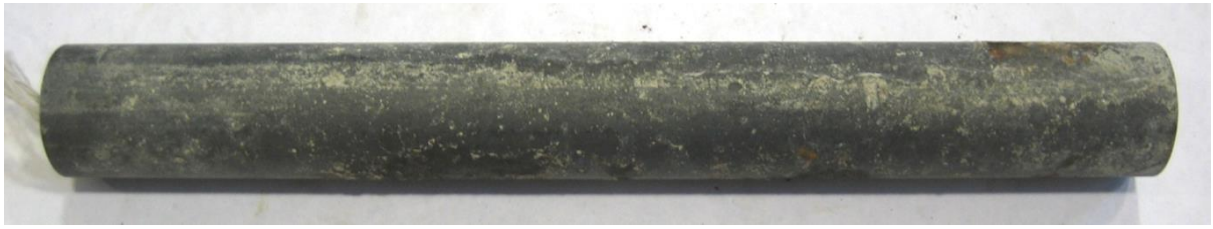

Source: FHWA.

Figure 55. Photo. Bottom side of the bar shown in figure 53.

Source: FHWA.

Figure 56. Photo. Close-up of a black bar.

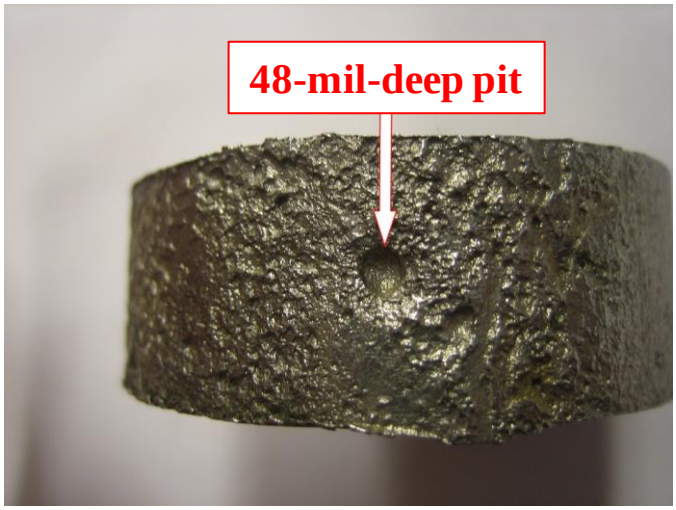

Source: FHWA.

Figure 57. Photo. A cleaned black bar segment exhibiting the deepest pit.

EC Bar Slab

Figure 58 shows the top surface of the EC bar slab that contained no visible cracks. Figure 59 shows the physical condition of the as-extracted EC bars in the same position and orientation as they were in the slab. All of the EC bars exhibited some localized corrosion. Again, the type 316L SS bar was clean without signs of corrosion.

Source: FHWA.

Figure 58. Photo. Top surface condition of EC bar slab before autopsy.

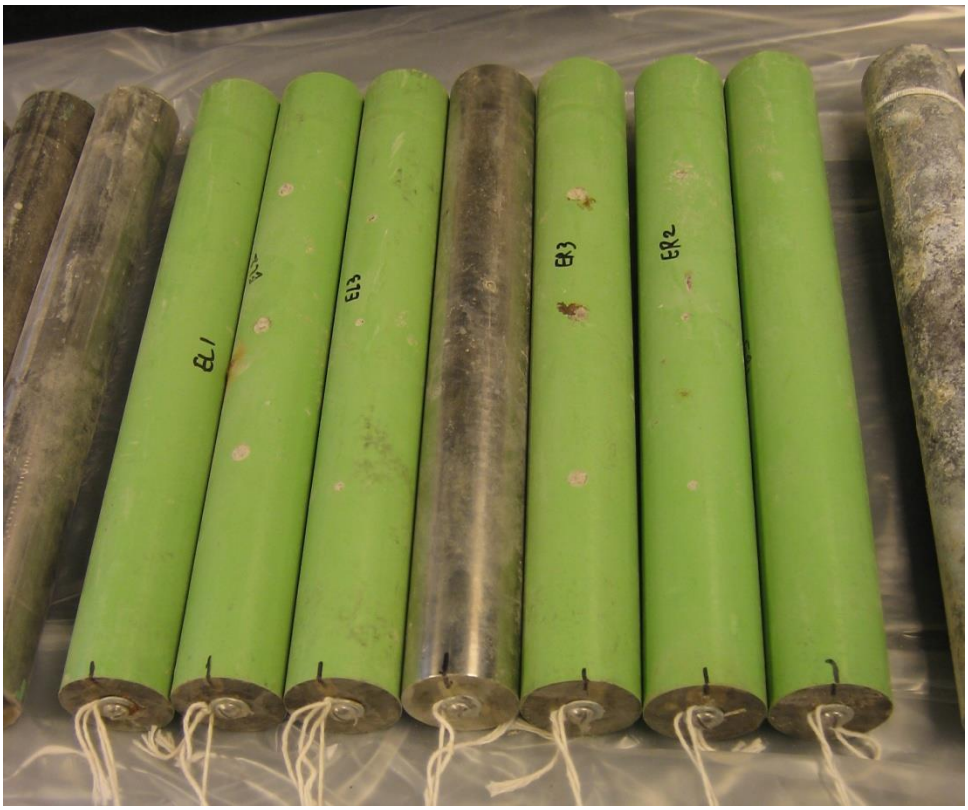

Source: FHWA.

Figure 59. Photo. Condition of as-extracted bars from EC bar slab.

Figure 60 through figure 62 show the initial condition, final condition right after extraction, and autopsied condition of an EC bar, respectively. It contained three holes of the large coating defect. The bar developed a localized corrosion near the middle defect, as shown in the small red square in figure 61. Upon removal of the rust-stained coating surface, severely corroded substrate was exposed (inset of figure 61). All of the loose coating on the same bar was removed using a knife as part of the autopsy work. The excessive coating disbondment that had occurred during the corrosion testing is revealed in figure 62. The disbonded areas that originated from the left and right defects exhibited fairly shiny surfaces, indicating that they were caused by a cathodic delamination process that produced hydroxyl ions. The extensive disbonded area around the middle defect was covered with red corrosion product, indicating that this area was one stage more advanced than the other defect areas; water, chloride ions, and oxygen reached the delaminated substrate and initiated corrosion there. The localized corrosion shown in figure 61 was associated with the substrate corrosion in question. As a coating disbonded area grew independently from the middle and the right defects, they eventually merged together to create one extensive coating delaminated area, as shown in figure 62.

Source: FHWA.

Figure 60. Photo. Initial condition of an EC bar (EL2).

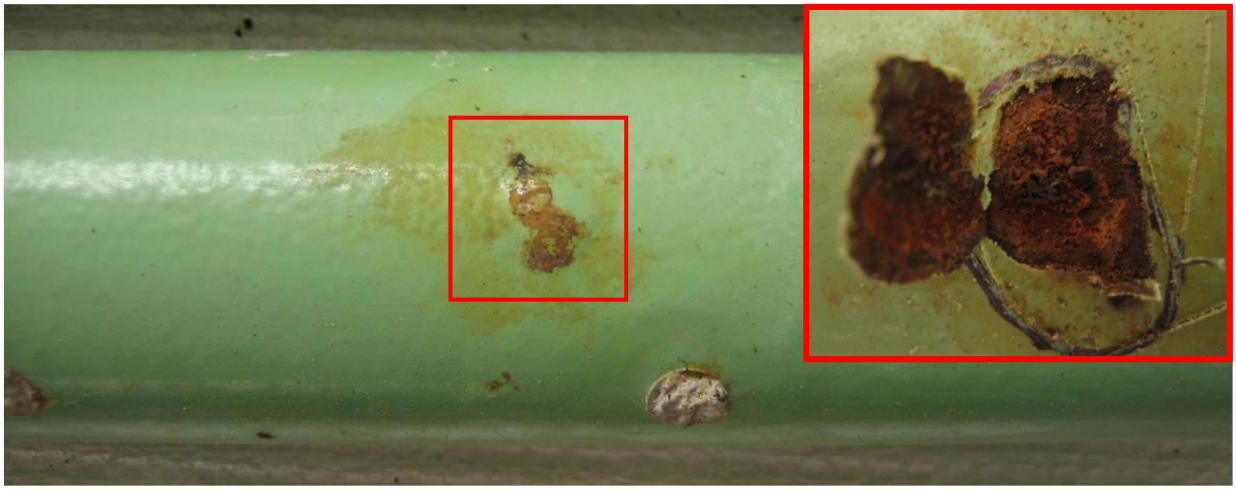

Source: FHWA.

Figure 61. Photo. As-extracted condition of the bar shown in figure 60.

Source: FHWA.

Figure 62. Photo. Autopsied condition of the bar shown in figure 61.

Figure 63 through figure 66 show a series of conditions of another EC bar containing the small coating defect. The bar did not exhibit visually abnormal conditions other than corrosion products covering the bar defect openings. When a low-voltage holiday detector was used to scan the surface, a large area of holiday clusters was identified, as marked in figure 65. When the loose coating was completely removed, another case of extensive coating disbondment connecting two defects was observed, as shown in figure 66. The exposed substrate exhibited various steel conditions from shinny to heavy corrosion product. It is noteworthy that the heavy corrosion product covered area corresponded fairly well to the holiday clustered area marked in figure 65.

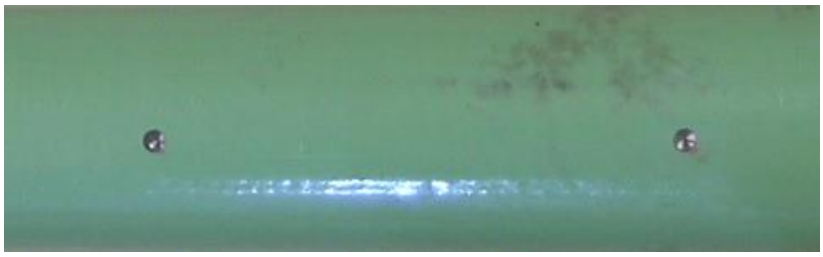

Source: FHWA.

Figure 63. Photo. Initial condition of another EC bar (EL3).

Source: FHWA.

Figure 64. Photo. As-extracted condition of the bar shown in figure 63.

Source: FHWA.

Figure 65. Photo. Deteriorated area of the bar shown in figure 64.

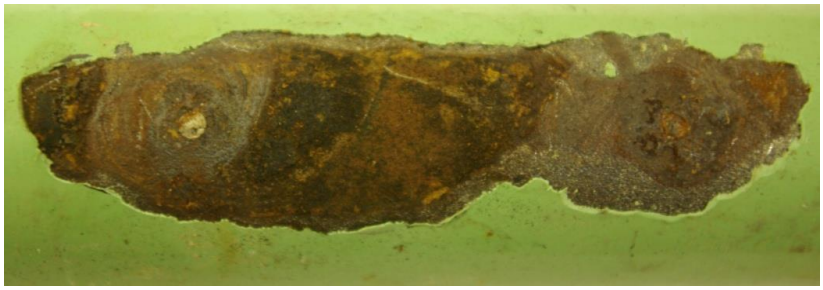

Source: FHWA.

Figure 66. Photo. Autopsied condition of the bar shown in figure 64 and figure 65.

HDG Bar Slab

Figure 67 shows the top surface of the HDG bar slab that contained no apparent visible cracks. Figure 68 shows the physical conditions of the as-extracted HDG bars in the same position and orientation as they were in the slab. All of the HDG bars exhibited white zinc oxide corrosion product and reddish steel corrosion product. The type 316L SS bar was clean without signs of corrosion.

Source: FHWA.

Figure 67. Photo. Top surface condition of HDG bar slab before autopsy.

Source: FHWA.

Figure 68. Photo. Condition of as-extracted bars from HDG bar slab.

Figure 69 shows the typical condition of an as-exposed HDG bar when the concrete was removed. Figure 70 shows the top side of the same bar upon its extraction. It shows intensive corrosion covered with black and reddish corrosion products near the simulated joint. A close-up view of such a condition is shown in figure 71. The bottom side of the bar shows mainly white zinc oxide corrosion product, as shown in figure 72. This condition indicates limited corrosion activity there.

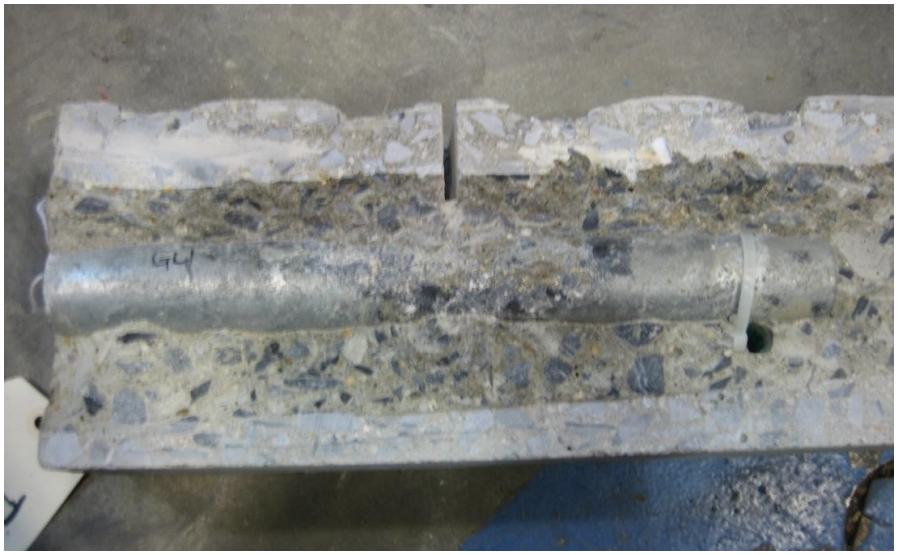

Source: FHWA.

Figure 69. Photo. Condition of an exposed HDG bar (GL1).

Source: FHWA.

Figure 70. Photo. Top side of the bar shown in figure 69.

Source: FHWA.

Figure 71. Photo. Close-up of the bar shown in figure 70.

Source: FHWA.

Figure 72. Photo. Bottom side of the bar shown in figure 69.

Figure 73 and figure 74 show another actively corroding spot covered with red corrosion product and no corrosion at an artificial large defect along the same bar (GL2), respectively. The absence of corrosion at the defect might be due to sacrificial cathodic protection offered by the zinc coating. Figure 75 shows a cleaned HDG bar piece that contained a 15-mil-deep pit surrounded by shallower pits. Since the galvanized zinc layer was completely penetrated, the red corrosion product of the steel substrate can be seen in the bottom of the deep pit.

Source: FHWA.

Figure 73. Photo. Close-up of another HDG bar (GL2).

Source: FHWA.

Figure 74. Photo. Another close-up of the bar shown in figure 73.

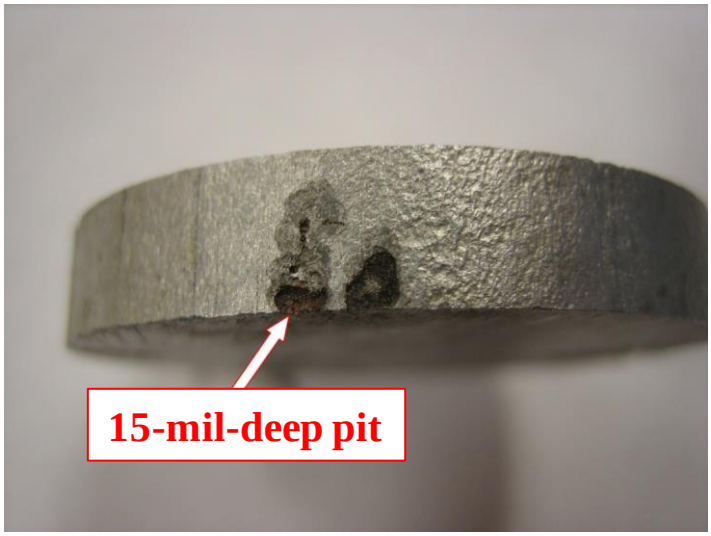

Source: FHWA.

Figure 75. Photo. A cleaned HDG bar section showing deep pits.

ZC Bar Slab

Figure 76 shows the top surface of the ZC bar slab that contained three small cracks. In addition, there was a weak white line that might be another young, small crack being developed. Figure 77 shows physical condition of the as-extracted ZC bars in the same position and orientation as they were in the slab. All of the ZC bars exhibited white zinc oxide and black corrosion products. The type 316L SS bar was clean with no corrosion.

Source: FHWA.

Figure 76. Photo. Top surface condition of ZC bar slab before autopsy.

Source: FHWA.

Figure 77. Photo. Condition of as-extracted bars from ZC bar slab.

Figure 78 shows an as-exposed ZC bar after the concrete was removed. Black corrosion product and nearby white corrosion product beneath the joint suggest that intensive corrosion took place. Such a condition appears to be worse than that of the HDG bars. Figure 79 shows a ZC bar/concrete interface that had a thick deposit of white and black corrosion products. Figure 80

and figure 81 show top and bottom sides of the as-extracted ZC bar shown in figure 78, respectively. Its top side shows intensive corrosion covered with black and white corrosion products, and the bottom side shows limited white corrosion product.

Source: FHWA.

Figure 78. Photo. Condition of an exposed ZC bar (ZR1).

Source: FHWA.

Figure 79. Photo. Bar/concrete interface for the bar shown in figure 78.

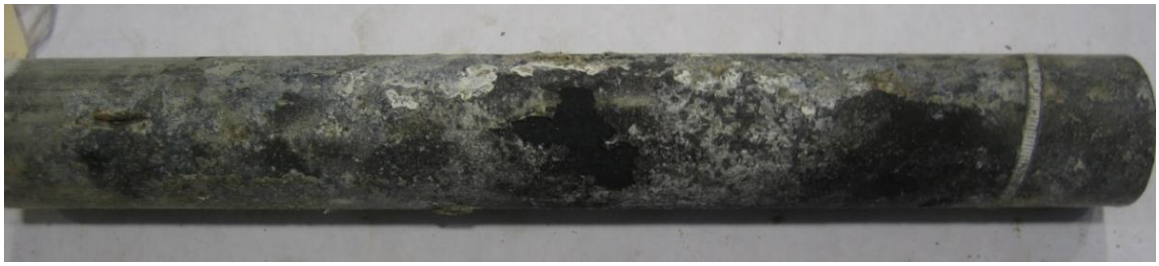

Source: FHWA.

Figure 80. Photo. Top side of the bar shown in figure 78.

Source: FHWA.

Figure 81. Photo. Bottom side of the bar shown in figure 78.

Figure 82 and figure 83 show another ZC bar (ZL1) exhibiting worse condition than the previous one on the ZR1 bar. Figure 82 reveals several noticeable pits in the black corrosion product covered area, and figure 83 shows a uniform white zinc corrosion product upon bar extraction that covered the entire bar/concrete interface with a mixture of white and black corrosion products beneath the joint. After viewing the physical condition of the extracted ZC bars and the bar/concrete interface, it is likely that the concrete cracks observed on the top surface are due to excessive corrosion products formed on the interface beneath the cracks.

Source: FHWA.

Figure 82. Photo. Condition of another exposed ZC bar (ZL1).

Source: FHWA.

Figure 83. Photo. Bar/concrete interface for the bar shown in figure 82.

Figure 84 and figure 85 show close-up views of a large defect and a small defect, respectively. Thanks to the sacrificial cathodic protection of the zinc cladding, none of the defects on the extracted ZC bars showed corrosion. However, figure 86 shows a representative pit that was found in the actively corroding zinc-cladding layer. There were many pits with various sizes and depths. Figure 87 shows a cross-section view of a severely corroded ZC bar. It can be seen that localized corrosion resulted in the compromised zinc-cladding layer with varying pit depths, and the deepest pit in the microphotograph almost reached the steel substrate.

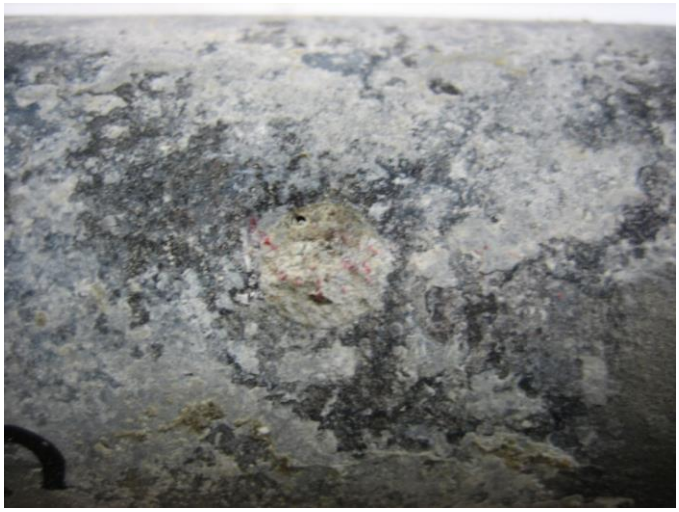

Source: FHWA.

Figure 84. Photo. Condition of a large defect.

Source: FHWA.

Figure 85. Photo. Condition of a small defect.

Source: FHWA.

Figure 86. Photo. Close-up of a deep pit.

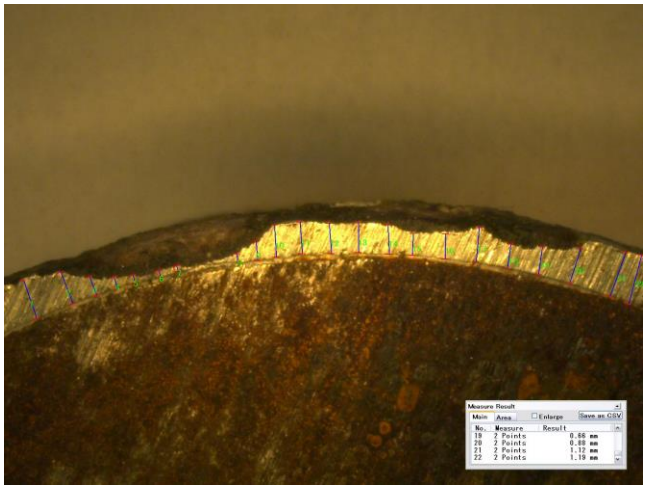

Source: FHWA.
Note: scale x200 magnification.

Figure 87. Photo. Cross-section of a corroded ZC dowel bar.

SCA/SCB Bar Slab

Figure 88 shows the top surface of the SCA and SCB bar slab that contained no apparent concrete cracks. Figure 89 shows the physical condition of the as-extracted SCA and SCB bars in the same position and orientation as they were in the slab. All of them exhibited superficial rust stains in some areas. The type 316L SS bar was clean without signs of corrosion.

Source: FHWA.

Figure 88. Photo. Top surface condition of an SCA/SCB bar slab before autopsy.

Source: FHWA.

Figure 89. Photo. Condition of as-extracted bars from SCA/SCB bar slab.

Figure 90 shows an as-extracted SCA bar containing the large defects. The middle defect developed corrosion, as seen in a close-up in figure 91. It is obvious from the heavy red corrosion product deposited around the defect hole that the CS core had been corroding. Corrosion at the middle defect must be closely related to proximity to the simulated joint. The top side of another as-extracted SCA bar containing the small defects is shown in figure 92. One of the defects was not filled with concrete but did not show corrosion, as shown in figure 93. Neither of the other defects showed corrosion.

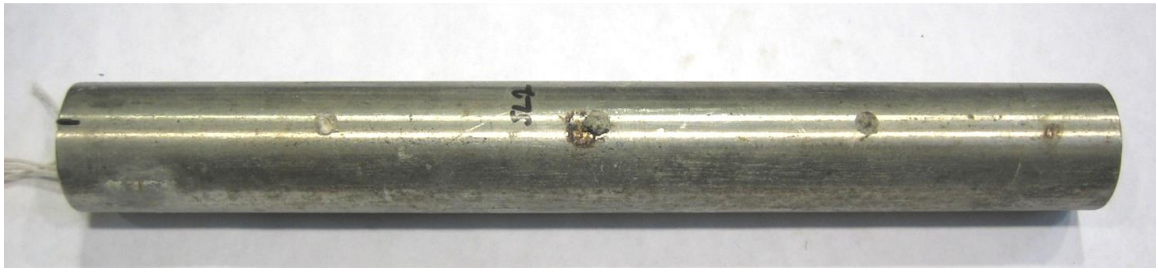

Source: FHWA.

Figure 90. Photo. Top side of an extracted SCA bar (SL2).

Source: FHWA.

Figure 91. Photo. Close-up of a corroding artificial defect on the bar shown in figure 90.

Source: FHWA.

Figure 92. Photo. Top side of another extracted SCA bar (SL3).

Source: FHWA.

Figure 93. Photo. Close-up of an artificial defect on the bar shown in figure 92.

Figure 94 shows the top side of an as-extracted SCB bar containing the large defects. This bar also developed corrosion in the middle defect, as shown in a close-up in figure 95. Similar to the

previous bar case, heavy corrosion product covered around the defect and CS core had been corroding due to its proximity to the simulated joint.

Source: FHWA.

Figure 94. Photo. Top side of an extracted SCB bar (SR2).

Source: FHWA.

Figure 95. Photo. Close-up of a corroding artificial defect on the bar shown in figure 94.

The corroding artificial defects confirmed that physical damage to the SC bars can lead to corrosion of the CS core. However, it seems unrealistic in any circumstance to introduce large perforated defects through such a hard SS-cladding layer in an attempt to simulate field conditions.

SCC Bar Slab

Figure 96 shows the top surface of the SCC bar slab that contained a large concrete crack above the black bar in the center. Figure 97 shows physical conditions of the as-extracted SCC bars and a black bar in the same position and orientation as they were in the slab. All of the SCC bars did not experience corrosion. However, the black bar exhibited severe corrosion.

Source: FHWA.

Figure 96. Photo. Top surface condition of the SCC bar slab before autopsy.

Source: FHWA.

Figure 97. Photo. Condition of the as-extracted bars from the SCC bar slab.

Figure 98 shows the condition of the black bar placed in the center of the slab soon after concrete was removed. Greenish and black corrosion products revealed that the bar went through intensive corrosion in the presence of chloride ions. A concrete fragment in the bottom of figure 98 shows a bar/concrete interface covered with thick corrosion product, which must have

cracked the slab above the black bar. Figure 99 and figure 100 show top and bottom sides of the extracted black bar. Corrosion was heavily concentrated on the top side.

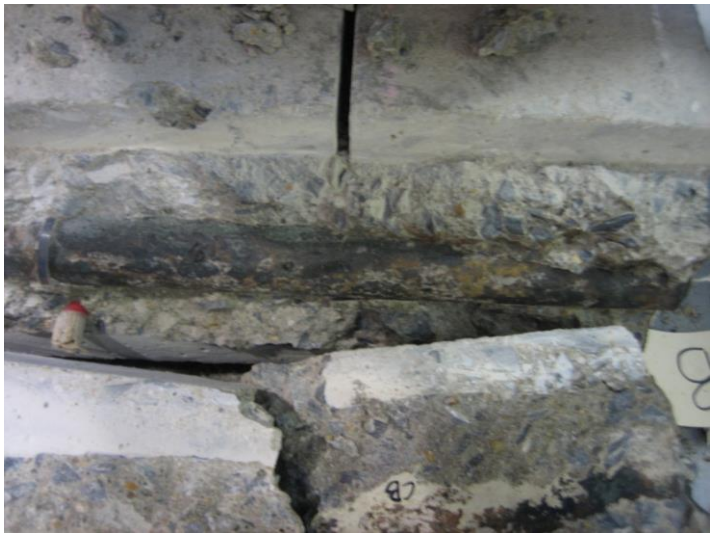

Source: FHWA.

Figure 98. Photo. Condition of the exposed black bar (CB).

Source: FHWA.

Figure 99. Photo. Top side of the bar shown in figure 98.

Source: FHWA.

Figure 100. Photo. Bottom side of the bar shown in figure 98.

Figure 101 shows an as-extracted SCC bar containing the large defects. This bar was the only one that showed minor rust stains at an artificial defect. This condition is shown in figure 102. The autopsied SCC bars indicate that a benefit of having epoxy coating as the second protective layer was questionable.

Source: FHWA.

Figure 101. Photo. Top side of an extracted SCC bar (CL2).

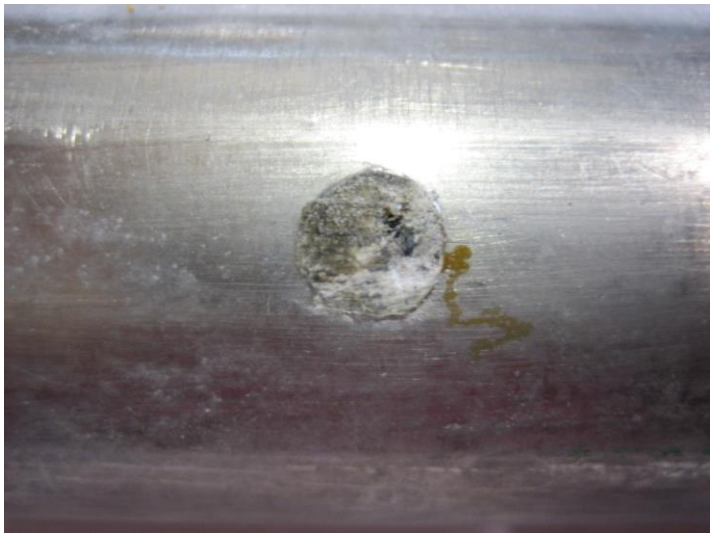

Source: FHWA.

Figure 102. Photo. Close-up of an artificial defect on the bar shown in figure 101.

Assorted Bar Slab

Figure 103 shows the top surface of the assorted bar slab that contained three concrete cracks. The longest crack developed was associated with the black bar. The second and third cracks from the right were linked to the HDG bar and the ZC bar, respectively. Figure 104 shows the physical condition of the as-extracted bars in the same position and orientation as they were in the slab. They exhibited similar corrosion morphologies as the same bar types extracted from their own slabs.

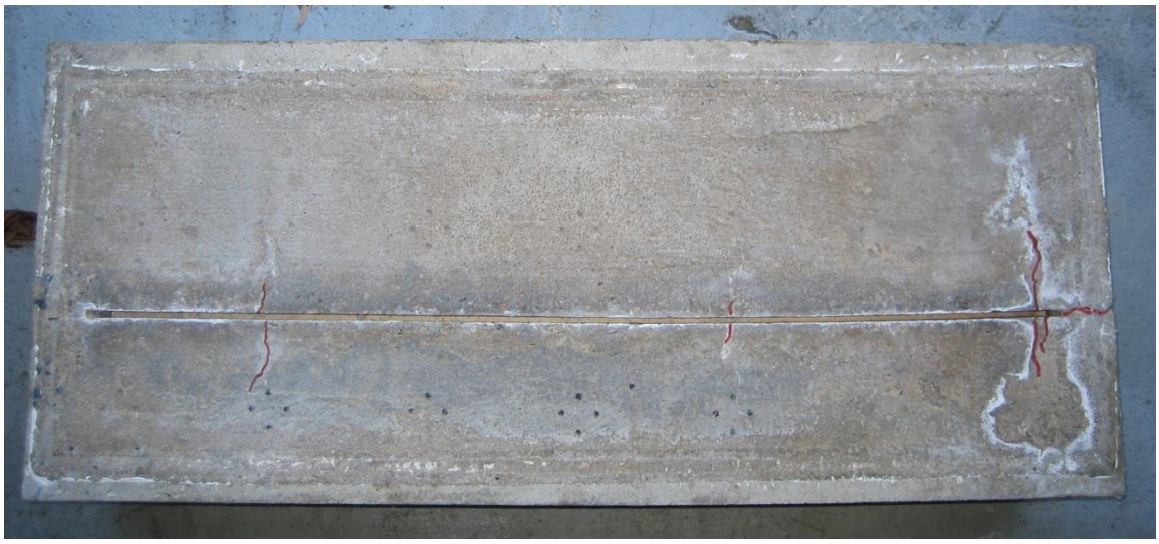

Source: FHWA.

Figure 103. Photo. Top surface condition of the assorted bar slab before autopsy.

Source: FHWA.

Figure 104. Photo. Condition of the as-extracted bars from the assorted bar slab.

Additional Comments

None of the extracted dowel bars' cut ends showed corrosion. Figure 105 shows the typical condition of the bar ends. This observation is understandable because chloride concentration

away from the simulated joint was relatively low. The present study does not have data to predict the corrosion behavior of the bare cut ends of various metallic dowel bars. This may be a topic of a follow-up study. Figure 106 shows the pristine condition of the type 316L solid SS dowel bar despite exposure to heavily chloride contaminated concrete (more than 11,000 ppm or 35 lb/yd^3 by weight of sample).

Source: FHWA.

Figure 105. Photo. Condition of bar cut ends.

Source: FHWA.

Figure 106. Photo. Clean condition of an exposed type 316L solid SS bar.

DISCUSSION

The uncoated black dowel bars used as a control in this study performed the poorest, as expected. Even though the cost of this material is the lowest, its life expectancy is too short to be cost effective.

The present study confirmed that type 316L solid SS dowel bars performed the best in the heavily chloride contaminated concrete. Three types of the SC dowel bars also showed equally

superior corrosion resistance in the same environment except at some artificial defects. In general, the latter is at least two times cheaper than the former while having similar corrosion resistance. SCC dowel bars did not yield supporting data that an additional epoxy-coating layer residing between the CS core and the SS cladding enhanced their corrosion resistance compared with the other SC bar types. To protect the bar ends from potential corrosion problems during an extended service life, it would be desirable to cover the CS core ends with semi-flexible plastic caps. Even though introduction of artificial damage into the SS cladding was done to be consistent with other coated bar materials, this type of damage turned out to be an unrealistic test condition because the SS is unlikely to be damaged to the levels that were investigated in this study during actual use, and thus, even the small defect size (0.07 percent) was judged to be unrealistic. Therefore, it is suggested that future studies should evaluate the SC dowel bars without intentional damage.

Based on these findings, the use of SCA dowel bars is recommended as the first choice of material among eight bar types to ensure durable pavement joints on heavily travelled roadways that cannot afford to have frequent repairs. SCB dowel bars can be an alternative if their producer can control the uniform target cladding thickness, which was not the case for the samples tested in the present study. Unfortunately, none of the SC dowel bar products are currently available in the market. It is hoped that these bars will be commercially available again in the future.

The corrosion performance data of the HDG and ZC dowel bars indicated that both zinc-based materials maintained very negative corrosion potentials and the highest macro-cell corrosion current among the bars tested, leading to rapid corrosion in the presence of heavy chloride concentration beneath the simulated pavement joints. The ZC dowel bars showed more active behavior than the HDG dowel bars. The different corrosion behavior between two bar types can be attributed to the fact that the latter is coated with pure zinc in a molten zinc bath, whereas the former was mechanically wrapped with a zinc alloy strip, which may have contained elements other than zinc. The autopsy results confirmed the non-destructively collected electrochemical data that the zinc layers were consumed quickly. The protective zinc layers were corroded over relatively large surface areas rather than localized galvanic corrosion around the artificial defects. As a result, the HDG dowel bars experienced heavy pitting corrosion and sometimes complete perforation of the zinc layer exposed near the joints. Some of the extracted HDG dowel bars exhibited red corrosion products, suggesting that the cathodic protection offered by the sacrificial zinc coating was no longer effective once the zinc layer was consumed and/or perforated. Thanks to much thicker zinc cladding, the ZC dowel bars did not exhibit the same level of surface deterioration as the HDG ones, except for localized areas near the joints. However, it is unlikely to provide adequate cathodic protection for the extended period of time (approximately 50 yr) after the zinc cladding is completely consumed and the CS core underneath is exposed. As a negative side effect of the excessive consumption of the zinc mass in a relatively short period of time, the ZC dowel bars tended to develop concrete cracks around them.

From these autopsy observations and the supporting corrosion performance data, it was concluded that thin zinc layer on the HDG dowel bars and even much thicker zinc cladding on the ZC bars are not adequate in the long-life pavements where prolonged and frequent

applications of heavy deicing salts is expected. Therefore, it is recommended that both zinc-based dowel bars be used only in mildly corrosive environments.

Overall, the EC dowel bars performed well in heavily chloride-contaminated concrete. Even though their corrosion potentials were sensitive to existing artificial defects and to newly developed defects while in the concrete, their corrosion performance, in terms of $i_{macro\text{-}cell}$ and the instantaneous rate of corrosion, was comparable to those of the SS dowel bars. They exhibited much higher electrical resistance compared with any other bar types, regardless of defect size. Moreover, none of the EC bars developed concrete cracks. Contrary to the excellent non-destructive evaluation data, the autopsy of the EC bars confirmed varying degrees of coating disbondment that mainly originated from the intentional coating damage. This is a well-known phenomenon for other epoxy-coated reinforcing (ECR) steel bar studies and other EC dowel bar studies, which observed the same problem.[4,5] Some of the delaminated areas revealed bright and clean steel substrate, whereas other areas experienced more advanced corrosion (i.e., rust stains through the lifted coating and the steel substrate covered with corrosion product). None of the extracted EC dowel bars exhibited the last stage of bar deterioration that has been typically characterized by heavy rust stains on the coating, numerous micro-cracks in the coating, brittle coating fragments, corroded steel substrate, and necking.[11,18] If the EC dowel bars had been tested for much longer, they would have eventually reached the final stage of deterioration. It is still unknown when this stage occurs and, hence, what will be the extended service life gained by the use of the EC dowel bars compared with other bar types. The total chloride concentration at the time of bar extraction exceeded 11,000 ppm (or 35 lb/yd^3), a very high level of chloride contamination even in in-service conditions. The best performing materials, regardless of the cost, were the SS bars. Furthermore, the likelihood of damaging a SS bar during installation is far less than damaging the epoxy coating. However, considering the absence of severe deterioration despite the elevated chloride contamination and the presence of excessive artificial coating defects, the overall corrosion resistance/cost was better for the ECR in relation to those of the other bar materials tested in this study.

A laboratory study investigating the corrosion behavior of disbonded ECR concluded that coating disbondment itself was not directly related to the corrosion performance of ECR in terms of macro-cell corrosion current.[26] It was reasoned that the epoxy coating, as a physical barrier and also an insulator, shielded the substrate from corrosion current flow in and out of the steel substrate. In other words, the disbonded coating can still function effectively to suppress the corrosion activity until the disbonded coating develops micro-cracks and permits corrosion current to flow. In fact, the significantly delaminated EC dowel bars (EL2 and EL3) exhibited negligible $i_{macro\text{-}cell}$ until the end of testing (figure 29).

Since the cost of the EC dowel bar is only 20 to 30 percent more than that of the black dowel bar and less than half of the SC dowel bars, the EC dowel bar is still a very attractive choice of material for the majority of existing pavements as well as new pavement construction. Its cost effectiveness can be further enhanced if the second-generation, high-quality, fusion-bonded epoxy coatings are used and stringent quality assurance (QA) and QC practices are implemented throughout the entire process, from proper coating application in the shop to transportation to storage to field installation at the construction sites. This practice should include diligent and thorough coating repair work in the field. When the EC dowel bars have minimal coating damage until the end of construction and are embedded in the high-quality concrete, extended

time-to-corrosion initiation ($t_{initiation}$) can be realized. This is because performance of the EC dowel bars is linked to the initial condition of the bars.[4] The use of the flexible plastic caps or field-applied coating and also the avoidance of welding to the basket (a prefabricated steel cage to which dowel bars are welded to form a long array of dowel bars) can protect the bar ends further from possible corrosion initiation.

In addition to offering an extended $t_{initiation}$, high-quality EC dowel bars without defects can also add much longer time-to-corrosion propagation ($t_{propagation}$) because there will be additional time earned during the coating deterioration process. Currently, it is believed that the EC dowel bars have 25- to 30-yr service lives.[4] When both extended $t_{initiation}$ and $t_{propagation}$ are considered, the EC dowel bars may be able to provide service lives comparable to the SS dowel bars and will be the most economical option until commercial SC dowel bars are available again with a massive production capability.

CHAPTER 5. CONCLUSIONS

The accelerated corrosion testing carried out under the present study created a severely corrosive environment for the metallic dowel bars. Such a harsh test condition yielded discernible performance differences among the eight bar materials tested. Based on the test results and data analysis, the following conclusions can be drawn:

- The best corrosion performance was achieved by the type 316L solid SS dowel bars. Three types of SC bars also exhibited superior corrosion resistance. Introduction of the large and small defects through the SS-cladding layer created corrosion of the CS core in some of the defect sites. However, this type of localized corrosion should be ignored because mechanical damage to the hard-cladding layer is unrealistic.

- The EC dowel bars also performed well in terms of macro-cell corrosion current density, instantaneous rate of corrosion, and AC resistance data. It behaved similarly to the SS bar types. However, the autopsied EC dowel bars revealed varying degrees of coating delamination and localized corrosion originating from some of the artificial coating defects. Despite this problem, EC dowel bars were able to suppress corrosion activities because of the shielding role of the coating, even bars suffered from coating disbondment, against corrosion current.

- As expected, the worst corrosion performance was observed with the uncoated CS dowel bars. Most of them produced the corrosion-induced concrete cracks.

- The HDG and ZC dowel bars are classified as the second-worst performance group. Even though the zinc-coating layers did their function well as the sacrificial cathodic protection systems for the bare steel exposed at the artificial defect sites, the consumption rates of the zinc mass were too excessive, leading to the premature depletion of the zinc layers in the areas with elevated chloride concentration. Some of the ZC dowel bars also produced concrete cracks around them. Therefore, these zinc-based dowel bars are recommended only for infrequently salted roadways and mild service conditions.

- For major roadways where repairs and/or traffic disruption are not feasible, high grades of solid SS dowel bars are recommended even though this means high initial costs. Considering the unavailability of the SC bars and the good performance of EC dowel bars at much lower price, it is recommended that high-quality EC dowel bars be continuously used in the majority of the major roadways subject to heavy deicing salts, provided that damage touchups and stringent QA/QC practices are implemented in the field to minimize initial coating defects, protecting the dowels until they are buried in concrete.

- Another study is recommended under dynamic loading conditions to evaluate complex behaviors of dowel materials in corrosive environments, particularly EC dowel bars with different physical conditions, including defect-free/high-quality bars that are conformed to the current specifications.

REFERENCES

1. Pavement Interactive. (2007). "*Jointed Plain Concrete Pavement*." (web page) Pavia Systems, Inc., Seattle, WA. Available online: http://www.pavementinteractive.org/article/jointed-plain-concrete-pavement, last accessed November 10, 2016.

2. Pavement Interactive. (2009). "*Jointed Reinforced Concrete Pavement*." (web page) Pavia Systems, Inc., Seattle, WA. Available online: http://www.pavementinteractive.org/article/jointed-reinforced-concrete-pavement, last accessed November 10, 2016.

3. Epoxy Interest Group, "*Epoxy-Coated Dowels for Concrete Pavement*." (web page) Epoxy Interest Group, Schaumburg, IL. Available online: http://www.epoxyinterestgroup.org/index.cfm/_api/render/file/?method=inline&fileID=732CDCB9-059F-5014-F2D119ABFC3D86D7, last accessed December 3, 2017.

4. Larson, R. and Smith, K.D. (2011), *Evaluation of Alternative Dowel Bar Materials and Coatings*, Report No. TPF-5(188), Ohio Department of Transportation, Columbus, OH. Available online: http://ntl.bts.gov/lib/43000/43200/43289/134411_FR.pdf, last accessed November 10, 2016.

5. McCallion, J.P. (1999). *FRP Dowel Bars—Analysis of Fiber Reinforced Polymer Dowels Removed From Active Roadways*. RJD Industries, Inc., Goleta, CA.

6. Federal Highway Administration. (2007). *Long-Life Concrete Pavements: Best Practices and Directions From the States*, Report No. FHWA-HIF-07-030, Federal Highway Administration, Washington, DC. Available online: http://www.google.com/url?sa=t&rct=j&q=&esrc=s&source=web&cd=1&ved=0CB4QFjAA&url=http%3A%2F%2Fwww.fhwa.dot.gov%2Fpavement%2Fconcrete%2Fpubs%2F07030%2F&ei=zoEpVf3SMs7uoATSs4DwBA&usg=AFQjCNGKhTjh_tOEfdMN7oLJKmCCtxpKiw&sig2=x4cgoMKJ3wpYGyGCjL5npQ, last accessed November 10, 2016.

7. Bischoff, D.L.B. (1996). *Random Skewed Joints With and Without Dowels*, Report No. WI/FEP-07-96, Wisconsin Department of Transportation, Madison, WI. Available online: http://wisdotresearch.wi.gov/wp-content/uploads/wifep-07-96skewedjoints.pdf, last accessed November 10, 2016.

8. CTC & Associates LLC. (2003). *Alternative Dowel Bar Materials for Concrete Pavement Joints*. Bureau of Highway Construction, Division of Transportation Infrastructure Development, Wisconsin Department of Transportation, Madison, WI. Available online: http://wisdotresearch.wi.gov/wp-content/uploads/tsrdowelbarmaterial.pdf, last accessed November 10, 2016.

9. Porter, M.L. and Guinn, Jr., R.J., (2002). *Assessment of Dowel Bar Research*, Report No. HR-1080, Iowa Department of Transportation, Iowa City, IA. Available online:

http://www.intrans.iastate.edu/reports/dowelbarsynthesis.pdf, last accessed November 10, 2016.

10. American Association of State Highway and Transportation Officials. (2006). *Standard Specification for Epoxy-Coated Reinforcing Bars: Materials and Coating Requirements*, M284, American Association of State and Highway Transportation Officials, Washington, DC.

11. Turgeon, C. (2003). *Minnesota's High Performance Concrete Pavements Evolution of the Practice*, Transportation Research Board 2003 Annual Meeting, Washington, DC.

12. Larson, R.M. and Smith, K.D. (2005). *Alternative Dowel Bars for Load Transfer in Jointed Concrete Pavements*, 8th International Conference on Concrete Pavements, Colorado Springs, CO.

13. American Association of State Highway and Transportation Officials. (2010). *Standard Specification for Corrosion-Resistant Coated Dowel Bars*, M254-06, American Association of State and Highway Transportation Officials, Washington, DC.

14. Snyder, M.B. (2005). *An Evaluation of Cathodically Protected Dowels for Concrete Pavements*, 8th International Conference on Concrete Pavements, Colorado Springs, CO.

15. ASTM A615/A615M. (2014). "Standard Specification for Deformed and Plain Carbon-Steel Bars for Concrete Reinforcement," *Book of Standards, 1.04*, AS TMaterials International, West Conshohocken, PA.

16. Battaglia, I.K. (2008). *Evaluation of MMFX 2 Steel Corrosion-Resistant Dowel Bars in Jointed Plain Concrete Pavement*, Report No. WI-03-08, Wisconsin Department of Transportation, Madison, WI. Available online: http://wisdotresearch.wi.gov/wp-content/uploads/wi-03-08dowelbars.pdf, last accessed Nov. 10, 2016.

17. ASTM A1035/A1035M. (2014). "Standard Specification for Deformed and Plain, Low-Carbon, Chromium, Steel Bars for Concrete Reinforcement," *Book of Standards, 1.04*, ASTM International, West Conshohocken, PA.

18. Mancio, M., Cruz, Jr., C., Zhang, J., Harvey, J.T., and Monteiro, P.J.M. (2007). *Laboratory Evaluation of Corrosion Resistance of Steel Dowels in Concrete Pavement*, Report No. UCPRC-RR-2005-10, University of California Davis and Berkeley, Pavement Research Center, Berkeley, CA. Available online: http://www.ucprc.ucdavis.edu/PDF/Corrosion%20Rpt%20UCPRC-RR-2005-10_Final.pdf, last accessed November 10, 2016.

19. ASTM A775/A775M. (2014). "Standard Specification for Epoxy-Coated Steel Reinforcing Bars," *Book of Standards, 1.04*, ASTM International, West Conshohocken, PA.

20. ASTM A934/A934M. (2014). "Standard Specification for Epoxy-Coated Prefabricated Steel Reinforcing Bars," *Book of Standards, 1.04*, ASTM International, West Conshohocken, PA.

21. ASTM C876. (2009). “Standard Test Method for Corrosion Potentials of Uncoated Reinforcing Steel in Concrete,” *Book of Standards, 3.02*, ASTM International, West Conshohocken, PA.

22. ASTM A1078/A1078M-12. (2012). “Standard Specification for Epoxy-Coated Steel Dowels for Concrete Pavement,” *Book of Standards, 01.04*, ASTM International, West Conshohocken, PA.

23. Washington State Department of Transportation. (2013). *Dowel Bars for New and Existing Concrete Pavements*. Construction Division, State Materials Laboratory, Washington State Department of Transportation, Seattle, WA. Available online: http://www.wsdot.wa.gov/NR/rdonlyres/43EF56B4-68AB-4465-87AC-A29826132144/0/DowelBarsfolio_Feb2013Final.pdf, last accessed Nov. 10, 2016.

24. ASTM A767/A767M. (2009). “Standard Specification for Zinc-Coated (Galvanized) Steel Bars for Concrete Reinforcement,” *Book of Standards, 1.04*, ASTM International, West Conshohocken, PA.

25. ASTM C1152 /C1152M-04. (2012). “Standard Test Method for Acid-Soluble Chloride in Mortar and Concrete,” *Book of Standards, 4.02*, ASTM International, West Conshohocken, PA.

26. Lee, S.K. (2008). *Characterizing Corrosion Behavior of Disbonded Epoxy Coated Reinforcing Steel–Updated Results*, NACE-08312, National Association of Corrosion Engineers International, New Orleans, LA.

HRDI-60/06-18(WEB)E